AMERICAN SOCIETY FOR MICROBIOLOGY | mSystems

Molecular and Cellular Biology | Research Article

Protein aggregation is a consequence of the dormancy-inducing membrane toxin TisB in *Escherichia coli*

Florian H. Leinberger,[1] Liam Cassidy,[2] Daniel Edelmann,[1] Nicole E. Schmid,[1] Markus Oberpaul,[3,4] Patrick Blumenkamp,[5] Sebastian Schmidt,[1] Ana Natriashvili,[6,7] Maximilian H. Ulbrich,[8,9] Andreas Tholey,[2] Hans-Georg Koch,[6] Bork A. Berghoff[1]

AUTHOR AFFILIATIONS See affiliation list on p. 21.

ABSTRACT Bacterial dormancy is a valuable strategy to survive stressful conditions. Toxins from chromosomal toxin-antitoxin systems have the potential to halt cell growth, induce dormancy, and eventually promote a stress-tolerant persister state. Due to their potential toxicity when overexpressed, sophisticated expression systems are needed when studying toxin genes. Here, we present a moderate expression system for toxin genes based on an artificial 5′ untranslated region. We applied the system to induce expression of the toxin gene *tisB* from the chromosomal type I toxin-antitoxin system *tisB/istR-1* in *Escherichia coli*. TisB is a small hydrophobic protein that targets the inner membrane, resulting in depolarization and ATP depletion. We analyzed TisB-producing cells by RNA-sequencing and revealed several genes with a role in recovery from TisB-induced dormancy, including the chaperone genes *ibpAB* and *spy*. The importance of chaperone genes suggested that TisB-producing cells are prone to protein aggregation, which was validated by an *in vivo* fluorescent reporter system. We moved on to show that TisB is an essential factor for protein aggregation upon DNA damage mediated by the fluoroquinolone antibiotic ciprofloxacin in *E. coli* wild-type cells. The occurrence of protein aggregates correlates with an extended dormancy duration, which underscores their importance for the life cycle of TisB-dependent persister cells.

IMPORTANCE Protein aggregates occur in all living cells due to misfolding of proteins. In bacteria, protein aggregation is associated with cellular inactivity, which is related to dormancy and tolerance to stressful conditions, including exposure to antibiotics. In *Escherichia coli*, the membrane toxin TisB is an important factor for dormancy and antibiotic tolerance upon DNA damage mediated by the fluoroquinolone antibiotic ciprofloxacin. Here, we show that TisB provokes protein aggregation, which, in turn, promotes an extended state of cellular dormancy. Our study suggests that protein aggregation is a consequence of membrane toxins with the potential to affect the duration of dormancy and the outcome of antibiotic therapy.

KEYWORDS toxin-antitoxin systems, type I toxins, protein aggregation, dormancy, antibiotics

Bacteria constantly encounter stressful conditions due to sudden changes in their environments. They can tolerate these stress conditions to some extent and can maintain cellular integrity by switching on designated response systems, which sense these conditions and adjust the expression of specific genes to counteract the harmful situation. Under extreme hostile conditions, however, regular stress response systems may fail to protect cells from lethal damages, a situation that is unpredictable and demands alternative survival strategies. One possibility is the formation of dormant cells, which are characterized by reduced cellular activity, growth arrest, and the ability to withstand even extreme stress conditions (1, 2). Dormancy typically occurs only in a

Editor Danielle Tullman-Ercek, Northwestern University, Evanston, Illinois, USA

Address correspondence to Bork A. Berghoff, bork.berghoff@uni-ulm.de.

The authors declare no conflict of interest.

See the funding table on p. 21.

Received 8 August 2024
Accepted 6 September 2024
Published 8 October 2024

fraction of cells and, therefore, represents an example of phenotypic heterogeneity that is considered a bet-hedging strategy for survival in unpredictable environments: some bacteria sacrifice their own propagation to ensure continuity of the genotype in case of extreme hostile conditions (3).

Bacterial dormancy occurs in different shapes and degrees and may therefore be defined as a "multidimensional trait space" (4). In its broadest definition, dormancy is "any rest period or reversible interruption of the phenotypic development of an organism" (5), which also includes myxospores within fruiting bodies of myxobacteria or endospores of some gram-positive bacteria, which may reside in dormant state for many years (6, 7). In contrast to these extreme morphotypes, bacterial populations almost constantly generate cells that are morphologically similar to their siblings but have entered a transient state of reduced activity from which they can rapidly recover. A prominent example are so-called persister cells, which are well known for their ability to survive antibiotic treatments (8–10). They have gained increasing attention as they may cause infection relapse or serve as a reservoir for antibiotic resistance development (11–13). As it stands right now, there are many ways into the persister state, including spontaneous events (14, 15), nutrient limitation and starvation (16, 17), metabolic perturbations (18), oxidative stress (19, 20), and low energy levels (21, 22). However, it is not entirely clear whether a combination of these events is necessary to reduce cellular activity to such an extent that persister formation is promoted. In this respect, not every dormant cell is a persister cell, but dormancy increases the likelihood of reaching the persister state (23).

Another possibility to induce dormancy is toxin-antitoxin (TA) systems, which are ubiquitously found in bacteria and contribute to stress responses or stabilization of mobile genetic elements (24, 25). Different TA system types have been identified, but they all have in common that the antitoxin inhibits toxin activity or prevents toxin production, which likely restricts toxin-dependent effects to specific (stress) conditions (24–28). Whether or not toxins from TA systems induce a persister state is subject to current debate (29, 30), but the contribution of toxins to bacterial dormancy and condition-dependent persister formation seems plausible (26, 31–33). One well-studied toxin with a potential influence on dormancy and persistence is TisB from the type I TA system *tisB/istR-1* in *Escherichia coli* (34–36). TisB is a small hydrophobic protein that targets the inner membrane and leads to membrane depolarization, ATP depletion, and further secondary effects, such as reactive oxygen species formation and inhibition of translation (31, 37–40). The reduced energy level in TisB-producing cells is expected to support persister formation, especially under conditions of DNA damage, when the corresponding *tisB* toxin gene is strongly induced upon auto-cleavage of the LexA repressor as part of the SOS response (33, 39, 41, 42). However, transcription of *tisB* is not sufficient to produce the TisB protein because the primary *tisB* mRNA (+1 mRNA) is translationally inactive due to an inhibitory secondary structure in its 5′ part. The +1 mRNA needs to undergo processing into the active +42 mRNA to be translated (43). Translation of the +42 mRNA depends on a non-canonical translation initiation mechanism that involves a single-stranded ribosome standby site (RSS), a 5′ pseudoknot structure, and ribosomal protein S1 (44, 45). However, the translation of +42 mRNA is efficiently inhibited by the RNA antitoxin IstR-1 (42, 43). Hence, two regulatory RNA elements (secondary structure in the +1 mRNA and antitoxin IstR-1) limit *tisB* expression to SOS conditions and set a threshold for TisB production in individual cells, thereby causing phenotypic heterogeneity (39, 46).

An early transcriptome study demonstrated that the heterologous production of TisB and other membrane toxins led to the induction of several stress response genes (47), indicating that these toxins cause stress due to primary and secondary effects (31, 40). However, heterologous toxin expression systems tend to produce excessive effects. In the current study, we aimed to construct a moderate expression system to study the TisB-dependent stress response. We observed that moderate *tisB* expression elicits a stress response that contributes to recovery from TisB-induced dormancy. Upregulation

of several chaperone genes suggested that TisB provokes protein aggregation, which was validated using a fluorescent reporter system. Intriguingly, we found that the DNA-damaging antibiotic ciprofloxacin causes protein aggregation in a TisB-dependent manner and that protein aggregates affect the dormancy duration of persister cells. Our study supports the view that TisB—and probably other type I toxins—affect dormancy and persistence through a variety of downstream effects, including protein aggregation.

RESULTS

A moderate expression system for investigation of TisB-induced dormancy

Production of the membrane toxin TisB from the type I TA system *tisB/istR-1* inflicts a stressful situation, including perturbation of membrane functioning, energy depletion, and further secondary effects (31, 48). Recent work on TisB has highlighted the importance of particular stress-related proteins in the context of TisB-dependent persistence, such as superoxide dismutases and alkyl hydroperoxide reductase (40, 49). To grasp the global response to TisB-mediated stress, we aimed to construct an inducible expression system that provokes TisB-dependent effects but avoids high TisB levels and concomitant TisB toxicity (37, 50). In *E. coli*, pBAD plasmids are applied for controllable gene expression from the P_{BAD} promoter using L-arabinose (L-ara) as an inducer. When using the pBAD derivative p+42-*tisB* (37), transcription from the P_{BAD} promoter produces the native *tisB* +42 mRNA, which is translationally active due to its accessible RSS and the existence of a Shine-Dalgarno (SD) sequence (Fig. 1A). However, *tisB* induction from p+42-*tisB* reduces the number of colony forming units (CFU) by at least 10-fold, indicating TisB toxicity and probably cell death (37). Since *tisB* expression from its chromosomal gene copy is not expected to cause cell death (37), but rather supports stabilization of a growth-arrested state (31), p+42-*tisB* does probably not represent a suitable expression system to study authentic TisB effects.

Expression strength can be modulated by plasmid copy number and promoter strength (51). Alternatively, the efficiency of translation can be modulated. We followed the latter strategy and tested an artificial 5′ UTR with a length of 20 bp that lacks an SD sequence (52) (Fig. 1A). The artificial 5′ UTR was fused to the *syfp2* open reading frame to analyze single-cell *syfp2* expression levels by flow cytometry. The SD-free 5′ UTR decreased the sYFP2 fluorescence by approximately 180-fold in comparison to an SD-containing 5′ UTR (Fig. S1). Importantly, the SD-free 5′ UTR did not introduce an expression heterogeneity among the population (Fig. S1). To test its suitability for moderate *tisB* expression, the native *tisB* 5′ UTR was replaced by the SD-free 5′ UTR to yield plasmid p0SD-*tisB*. Using 3×FLAG fusions and western blot analysis, we compared the p+42-*tisB* and p0SD-*tisB* systems by assessing 3×FLAG-TisB protein levels in *E. coli* wild-type (WT) MG1655 (Fig. 1B). 3×FLAG-TisB levels were reduced by ~10-fold using the p0SD-*tisB* system, which was presumably due to lower efficiency of translation initiation but might also be partly attributable to lower steady-state levels of the *0SD-3×FLAG-tisB* mRNA (Fig. S1). Optical density (OD_{600}) measurements demonstrated that TisB induction from plasmid p0SD-*tisB* by L-ara was sufficient to halt cell growth during the exponential phase, while an empty pBAD control showed normal growth (Fig. 1C). There was, however, a short delay for growth inhibition with p0SD-*tisB* when compared to p+42-*tisB*. The primary effect of TisB is depolarization of the inner membrane (38, 39). We assessed depolarization by the potential-sensitive probe $DiBAC_4(3)$ after 1 hour of L-ara treatment during the exponential phase. Expression from both p+42-*tisB* and p0SD-*tisB* caused an increase in intracellular $DiBAC_4(3)$ fluorescence in comparison to the empty pBAD control as assessed by flow cytometry (Fig. 1D). While the main population was similarly shifted with both expression systems, a second population with an increased $DiBAC_4(3)$ fluorescence occurred, which was especially prominent with the p+42-*tisB* system. Whether this subpopulation represents extremely damaged or even dead cells remains unknown. Importantly, after 1 hour of L-ara treatment, 66% of cells were able to form colonies with the p0SD-*tisB* system, while this value dropped to 1% with p+42-*tisB* (Fig.

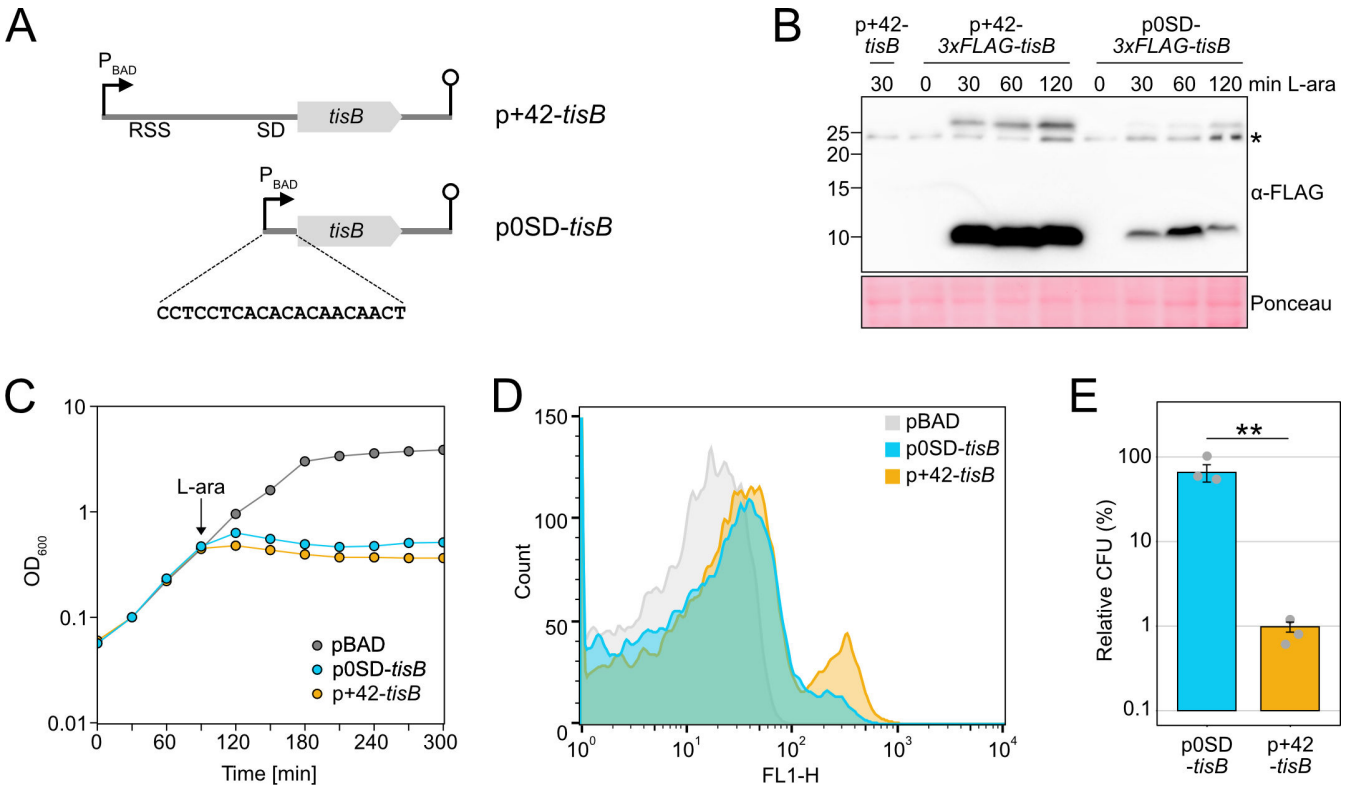

FIG 1 Characterization of a moderate *tisB* expression system. (A) Schematic representation of different *tisB* expression systems. The p+42-*tisB* plasmid contains the native *tisB* 5′ UTR, including a RSS and a SD sequence. Transcription from the P_{BAD} promoter starts at the *tisB* +42 position. The p0SD-*tisB* plasmid contains the *tisB* coding sequence preceded by an artificial 20 bp 5′ UTR. Lollipop structures indicate Rho-independent terminators. (B) Detection of 3×FLAG-TisB. Wild-type MG1655 harboring 3×FLAG-tag variants of p+42-*tisB* and p0SD-*tisB* were grown to an OD_{600} of ~0.4 (exponential phase) and treated with L-ara (0.2%). Samples were collected at the indicated time points. Total protein was separated using Tricine-SDS-PAGE and transferred to PVDF membranes by electro-blotting. 3×FLAG-TisB was detected using an HRP-conjugated monoclonal α-FLAG antibody. As a negative control, p+42-*tisB* was used. Two TisB-specific bands are visible, one at ~10 kDa and one above 25 kDa. The asterisk indicates an unspecific band. Ponceau staining is shown as loading control. (C) Growth inhibition by TisB. Wild-type MG1655, harboring p0SD-*tisB*, p+42-*tisB* or an empty pBAD plasmid, was treated with the inducer L-ara (0.2%) at an OD_{600} of ~0.4 (exponential phase; arrow). The OD_{600} was measured over time. Data points indicate the mean of three biological replicates. (D) TisB-dependent membrane depolarization. Wild-type MG1655 cells, harboring p0SD-*tisB*, p+42-*tisB* or an empty pBAD plasmid, were treated with the inducer L-ara (0.2%) for 1 hour when an OD_{600} of ~0.4 was reached (exponential phase). Staining with the potential-sensitive probe $DiBAC_4(3)$ was applied to assess depolarization. $DiBAC_4(3)$ fluorescence was measured using flow cytometry and the FL1-H detector. 10,000 events are displayed for each strain. (E) TisB toxicity with different expression systems. Wild-type MG1655, harboring p0SD-*tisB* or p+42-*tisB* was treated with L-ara (0.2%) during the exponential phase (OD_{600} ~0.4) for 1 hour. Pre- and post-treatment samples were used to determine relative CFU (%). Bars represent the mean of three biological replicates and error bars indicate the standard deviation. Dots show individual data points. ANOVA with post-hoc Tukey HSD test was performed (**$P < 0.01$).

1E). These findings indicate that p0SD-*tisB* largely avoids TisB toxicity and, therefore, represents a suitable expression system to study TisB-induced dormancy.

Dynamic phenotypic features upon moderate *tisB* expression

Elevated toxin levels were shown to increase phenotypic heterogeneity with respect to growth-arrest duration and persistence time (39, 53). The duration of toxin-induced growth arrest is reflected by the time that is needed by single cells to form colonies on agar plates, which can be quantified using the ScanLag method (54, 55). When *E. coli* wild-type MG1655, containing p0SD-*tisB*, was grown to an OD_{600} of ~0.4 (exponential phase) and plated on regular LB agar plates without L-ara (T0; Fig. 2A), the median colony appearance time was 820 min (Fig. 2B). The narrow appearance-time distribution indicated homogeneous lag times, as expected from exponentially growing populations. By contrast, when cultures were treated with L-ara for 30 min to induce TisB-dependent growth arrest before cells were spread on agar plates (T30; Fig. 2A), the median colony

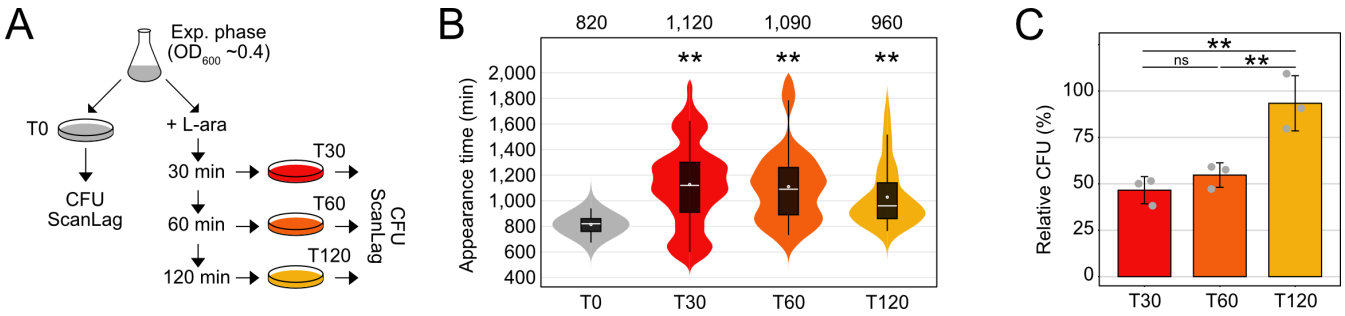

FIG 2 Dynamic phenotypic features upon moderate *tisB* expression. (A) Schematic representation of the performed experiment. Wild-type MG1655, harboring the p0SD-*tisB* plasmid, was treated with L-ara (0.2%) in the exponential phase (OD_{600} ~0.4). At the indicated time points (T30, T60, and T120), cells were plated on LB agar without L-ara and colony growth was analyzed using the ScanLag method (see Material and Methods). As a control, cells were analyzed before L-ara was added (T0). (B) ScanLag analysis was applied to determine the colony appearance time after *tisB* expression. For each time point, colony appearance times are illustrated as violin box plots. Colonies from three biological replicates were combined (T0: n = 154; T30: n = 59; T60: n = 103; T120: n = 124). The white dot indicates the mean. The respective median appearance time (white bar) is shown on top of each plot. L-ara-treated samples were compared to the control (T0) using a pairwise Wilcoxon rank-sum test (**P < 0.0001). (C) Colony counts increase upon progressing *tisB* expression. LB agar plates from panel B were used to determine colony counts. Pre-treatment (T0) and post-treatment (T30, T60, and T120) samples were used to determine relative CFU (%). Bars represent the mean of three biological replicates and error bars indicate the standard deviation. Dots show individual data points. ANOVA with *post hoc* Tukey HSD test was performed (**P < 0.01; ns: not significant).

appearance time shifted to 1,120 min. In other words, cells needed on average 5 hours longer to form colonies. Furthermore, heterogeneity of colony appearance was clearly increased (Fig. 2B). Since the speed of colony growth could not account for the 5-hour shift (Fig. S2), we concluded that TisB production from the p0SD-*tisB* system generated populations with very heterogeneous growth-arrest durations. While results for a 60 min L-ara treatment (T60) were comparable to the 30-min time point, the median colony appearance time was only 960 min after 120 min of L-ara treatment (T120), which was also accompanied by a more homogeneous distribution (Fig. 2B). Intriguingly, relative CFU counts stayed at ~50% during the first 60 min of L-ara treatment but increased to more than 90% after 120 min (Fig. 2C). Hence, cells regained their ability to form colonies at later stages of the experiment. Even though the p0SD-*tisB* plasmid was stable over the whole duration of the experiment (Fig. S1), we observed changes in 3×FLAG-TisB levels, with a peak at 60 min and a decline at 120 min (Fig. 1B), which was mirrored at the mRNA level (Fig. S1). This might represent an inconsistent expression strength introduced by the p0SD-*tisB* system itself. Alternatively, the decline in TisB protein levels and the improved ability to form colonies at the 120 min time point indicate an adaptation, probably through activation of a stress response that limits further TisB production.

A global transcriptome analysis reveals TisB-dependent upregulation of stress-related genes

It has already been observed that type I toxins cause upregulation of several stress-related genes (47), and we have shown that *tisB* expression provokes superoxide formation and upregulation of *soxS* and the SoxRS regulon (40). To reveal the response to TisB on a global scale, transcriptome analysis of MG1655 p0SD-*tisB* was performed. Cultures were grown to an OD_{600} of ~0.4 (exponential phase) and treated with L-ara for 30 min. Samples before and after L-ara treatment were collected and analyzed by RNA-seq, which identified 67 upregulated and 66 downregulated genes (log_2 fold change > 2 and < −2, P-value < 0.01; Data Set S1). We specifically focused on upregulated genes, as they might represent an active response to TisB. As expected, *tisB* and *soxS* were among the genes with the strongest upregulation (Fig. 3A). To select candidates for further analysis, we compared the set of upregulated genes from our RNA-seq analysis to (i) microarray data of heterologous *tisB* expression (47), (ii) proteome data of a de-regulated *tisB* strain (49), and (iii) transcriptional regulation data from the RegulonDB database

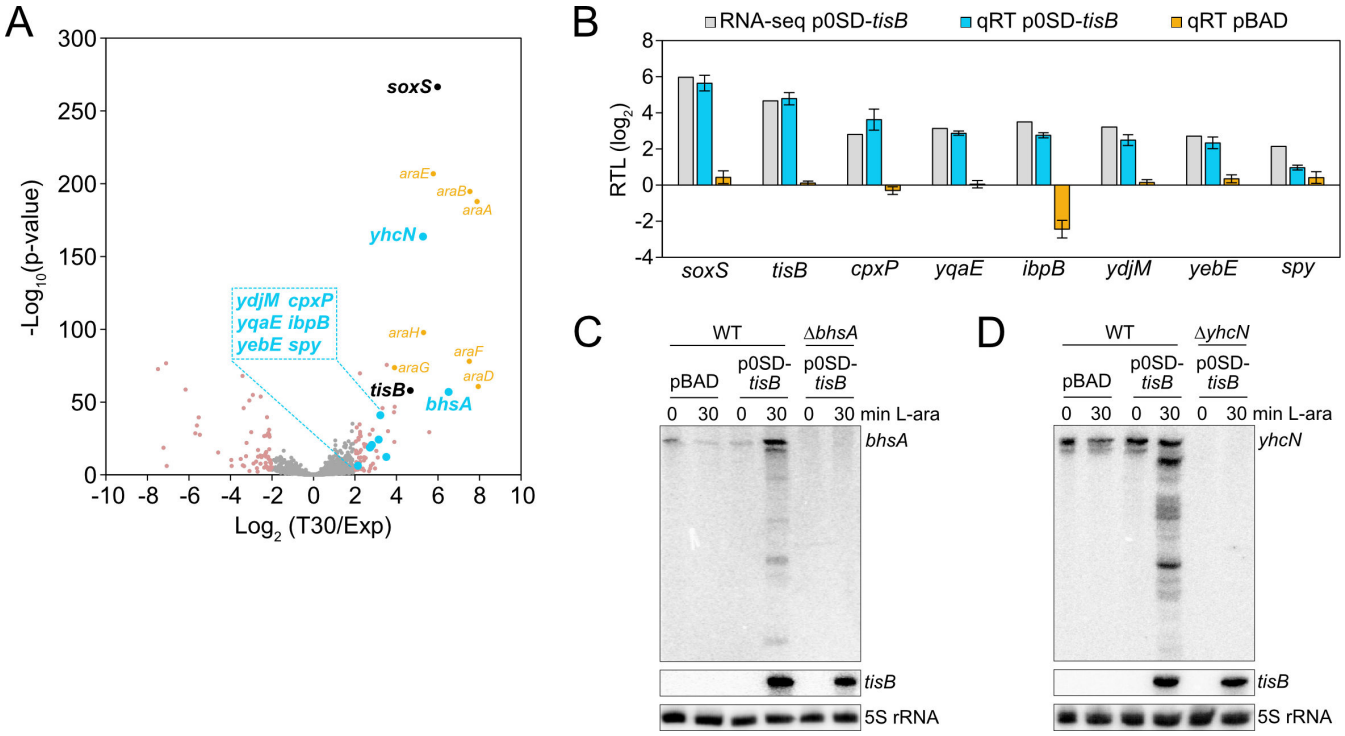

FIG 3 Identification of TisB-responsive genes by RNA-seq. (A) Global response to *tisB* expression. Wild-type MG1655, harboring the p0SD-*tisB* plasmid, was treated with L-ara (0.2%) during the exponential phase (OD_{600} ~0.4) for 30 min. RNA samples extracted before (Exp) and after treatment (T30) were analyzed using RNA-seq. The volcano plot illustrates the $\log_2$ fold change on the *x*-axis and the $-\log_{10}$(*P*-value) on the *y*-axis. Differentially expressed genes ($\log_2$ fold change > 2 or < −2, *P*-value < 0.01) are shown in pink. Selected candidates are highlighted in blue, while genes affected by L-ara are shown in orange (*araBAD*, *araE*, *araFGH*), and *tisB* and *soxS* are shown in black. (B) Confirmation of RNA-seq using qRT-PCR. Wild-type MG1655, harboring p0SD-*tisB* (blue bars) or an empty pBAD plasmid (orange bars), was treated with L-ara (0.2%) during exponential phase (OD_{600} ~0.4) for 30 min. Relative transcript levels (RTL; $\log_2$) were assessed by qRT-PCR (qRT). $\log_2$ fold changes from the RNA-seq analysis are shown for comparison (gray bars). Bars represent the mean of three biological replicates, with two technical replicates each, and error bars indicate the standard deviation. (C, D) Confirmation of RNA-seq using northern blot analysis. Wild-type MG1655, harboring p0SD-*tisB* or an empty pBAD plasmid, was treated with L-ara (0.2%) during the exponential phase (OD_{600} ~0.4) for 30 min. Total RNA was separated using urea-polyacrylamide gels and blotted onto nylon membranes. Radioactive probes binding to the coding region of (C) *bhsA* or (D) *yhcN* were applied for the detection of transcripts. Corresponding deletion mutants (Δ*bhsA* or Δ*yhcN*) were used to show the specificity of the probes. A *tisB* probe was applied to verify *tisB* induction from p0SD-*tisB*, and 5S rRNA was probed as loading control.

(56). The regulon analysis highlighted genes that are transcriptionally regulated by CpxR, the response regulator from the CpxAR two-component system (Fig. S3). The Cpx system belongs to the envelope stress response and is mainly involved in sensing misfolded proteins in the inner membrane and periplasm (57). In total, we selected four CpxR-dependent genes: *cpxP*, *spy*, *yebE,* and *yqaE* (Fig. 3A). Importantly, *cpxP*, *spy,* and *yebE* were found in the transcriptome study by Fozo et al. (47), and *spy* and *yebE* were also found in the proteome study by Spanka et al. (49). CpxP and Spy are located in the periplasm and have chaperone functions; YebE and YqaE are poorly characterized inner membrane proteins. In addition, we selected *ydjM* (Fig. 3A), encoding another poorly characterized inner membrane protein. Like *tisB*, *ydjM* belongs to the LexA regulon and might have an important function during the SOS response. The transcriptome study by Fozo et al. showed that the *ibpAB* operon is upregulated upon type I toxin expression (47). Both *ibpA* and *ibpB* encode small heat-shock proteins (sHSPs) with chaperone functions in the cytoplasm. Since *ibpB* showed stronger induction than *ibpA* in our RNA-seq data (Data Set S1), we selected *ibpB* for further analysis (Fig. 3A). We applied quantitative reverse transcription PCR (qRT-PCR) to verify TisB-dependent induction of the selected genes. *soxS* and *tisB* were used as positive controls (Fig. 3B). To exclude that upregulation of stress-related genes was due to the L-ara treatment, wild-type MG1655

containing an empty pBAD plasmid was analyzed by qRT-PCR, clearly showing that L-ara alone was not sufficient to cause induction of the stress-related genes (Fig. 3B). Finally, *bhsA* and *yhcN* were selected because they were among the genes with the strongest upregulation (Fig. 3A). Both genes encode DUF1471 domain-containing proteins that are located in the cell envelope and have a putative role in stress responses and/or biofilm formation (58–60). Since qRT-PCR analysis did not produce reliable results for *bhsA* and *yhcN*, northern blot analysis was performed, which confirmed their TisB-dependent induction (Fig. 3C and D). We note, however, that *tisB* expression caused accumulation of several mRNA degradation products, which was particularly evident for *yhcN* (Fig. 3D). Strong *tisB* expression causes rRNA degradation in less than 1 hour (37, 40, 50), but this was not observed when using the p0SD-*tisB* system (Fig. S1), suggesting that global RNA decay cannot account for *bhsA* and *yhcN* degradation. Degradation of *bhsA* and *yhcN* might have a biological function, such as the generation of regulatory RNAs, but this needs further investigation.

Stress-related genes support recovery from TisB-induced dormancy

To evaluate the function of the selected candidates with respect to TisB-induced dormancy, we deleted the corresponding genes and transferred the p0SD-*tisB* plasmid to the resulting mutants. As expected, all mutants showed L-ara-induced and TisB-dependent growth inhibition (Fig. S4). In a subsequent experiment, mutants were grown to an OD_{600} of ~0.4 (exponential phase) and tested for their ability to form colonies after 1 hour of L-ara treatment. The relative CFU counts for the mutants ranged between 43% and 111%, which was not strikingly different when compared to the wild type (70%; Fig. 4A). We concluded that each gene only had a minor influence on the ability of TisB-producing cells to form colonies on LB agar plates. We reasoned that the stress-related genes might rather influence the growth-arrest duration by supporting the recovery from TisB-mediated stress (40, 49). Indeed, when using ScanLag, seven out of eight mutants showed a delayed recovery and significantly increased growth-arrest duration in comparison to the wild type, with Δ*bhsA* being the only exception (Fig. 4B). The growth-arrest duration, as measured by the colony appearance time, was prolonged by at least 80 min (Δ*ibpB*) and up to 220 min (Δ*yebE* and Δ*cpxP*). To exclude that the gene deletion itself and/or the L-ara treatment would affect the colony appearance time, an empty pBAD plasmid was transferred to the mutants. The resulting strains were grown to the exponential phase, treated with L-ara for 1 hour, and analyzed by ScanLag. In this control experiment, none of the mutants showed a delayed colony appearance in comparison to the wild type (Fig. S5), clearly indicating that the stress-related genes have a particular function upon TisB-mediated stress and probably support the recovery process. Since four of the eight candidates belong to the CpxR regulon (Fig. 4A), we constructed a *cpxR* deletion mutant, transferred the p0SD-*tisB* plasmid, and induced *tisB* expression by L-ara. However, neither CFU counts nor colony appearance were significantly different in the *cpxR* mutant when compared to the wild type (Fig. S6), probably due to the dual regulatory function of CpxR and the complex features found within the CpxR regulon (61).

TisB causes intracellular ATP depletion and protein aggregation

The importance of proteins with chaperone activity during recovery from TisB-induced growth arrest (Fig. 4) suggested that unfolded proteins and protein aggregates impose a challenge for TisB-producing cells. It was previously demonstrated that due to ATP depletion, protein aggregates form and affect the dormancy of bacterial cells (62, 63). Since TisB is expected to decrease the intracellular ATP concentration due to depolarization of the inner membrane and breakdown of the proton motive force (33, 35, 37), intracellular ATP concentrations were measured before and after L-ara treatment in wild-type MG1655 containing either p0SD-*tisB* or an empty pBAD plasmid. In the TisB-producing strain, a 60-min treatment with L-ara caused a ~32-fold ATP reduction, while the ATP concentration remained unchanged in the control strain (Fig. 5A). To assess

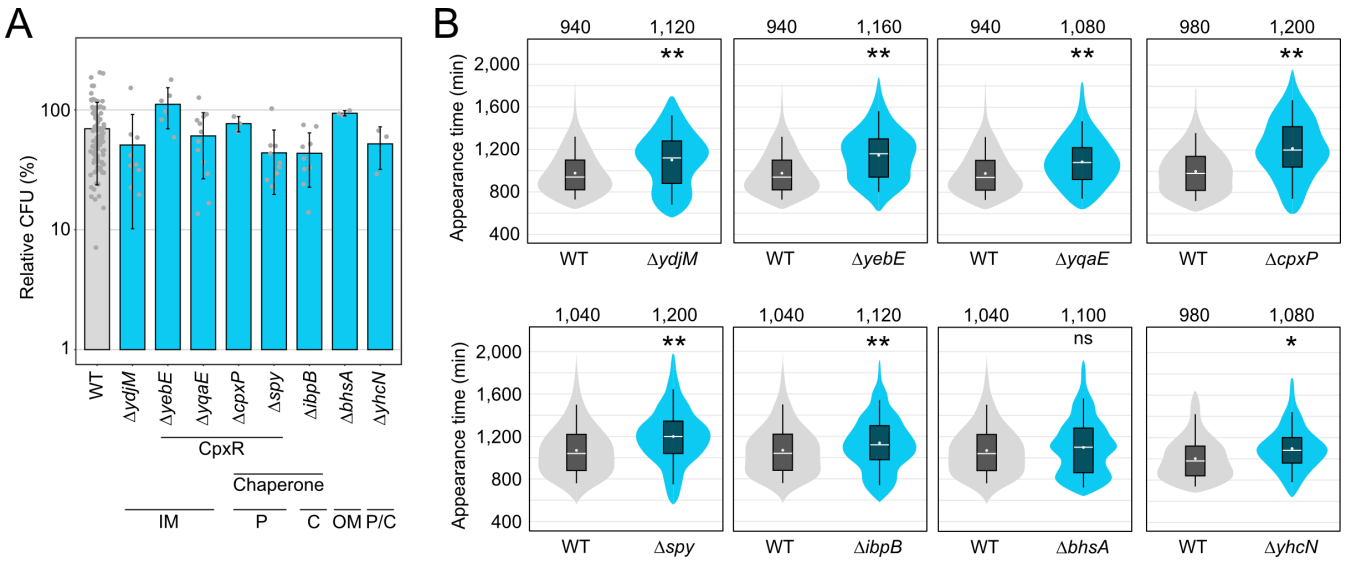

FIG 4 TisB-responsive genes mainly affect the recovery after *tisB* expression. (A) TisB toxicity in selected deletion mutants. WT MG1655 and deletion mutants, harboring the p0SD-*tisB* plasmid, were treated with L-ara (0.2%) during the exponential phase (OD_{600} ~0.4) for 1 hour. Pre- and post-treatment samples were used to determine relative CFU (%). Bars represent the mean of at least three biological replicates and error bars indicate the standard deviation. Dots show individual data points (WT: n = 102; Δ*ydjM*: n = 9; Δ*yebE*: n = 6; Δ*yqaE*: n = 12; Δ*cpxP*: n = 3; Δ*spy*: n = 9; Δ*ibpB*: n = 9; Δ*bhsA*: n = 3; Δ*yhcN*: n = 3). ANOVA with post hoc Tukey HSD was performed (no significant difference between deletion mutants and the wild type was detected). It is indicated whether the genes are CpxR-dependent or have a chaperone activity. Their proposed cellular localization is given (C: cytoplasm, IM: inner membrane, P: periplasm, OM: outer membrane). (B) ScanLag analysis of selected deletion mutants. WT MG1655 and deletion mutants, harboring the p0SD-*tisB* plasmid, were treated with L-ara (0.2%) during the exponential phase (O_{D600} ~0.4) for 1 hour. ScanLag was applied to determine the colony appearance time after *tisB* expression. For each deletion mutant, colony appearance times are illustrated as violin box plots and compared to a corresponding wild type. Colonies from at least three biological replicates were combined (WT: $n \geq 192$; Δ*ydjM*: n = 452; Δ*yebE*: n = 383; Δ*yqaE*: n = 393; Δ*cpxP*: n = 252; Δ*spy*: n = 356; Δ*ibpB*: n = 682; Δ*bhsA*: n = 365; Δ*yhcN*: n = 192). The white dot indicates the mean. The respective median appearance time (white bar) is shown on top of each plot. Deletion mutants were compared to wild-type MG1655 using a pairwise Wilcoxon rank-sum test (*P < 0.001, **P < 0.0001, ns: not significant). It should be noted that ScanLag results vary between individual runs. For every mutant, statistical testing refers to the corresponding control strain (WT) from the same experimental run.

cytosolic protein aggregation as a likely consequence of ATP depletion, we applied a reporter strain that chromosomally expresses a monomeric superfolder green fluorescent protein (msfGFP) fused to the C-terminus of the sHSP IbpA (64). As expected, cytosolic msfGFP fluorescence changed from a diffuse to a punctuated pattern (i.e., formation of foci) after 15 min of heat shock at 47°C (Fig. S7). Since IbpA localizes to protein aggregates, the msfGFP foci clearly indicated the formation of protein aggregates in the cytoplasm due to elevated temperature (63, 64). We performed a U-Net analysis (65) to count msfGFP foci in individual cells (Fig. S7). Expression of *tisB* from p0SD-*tisB* in the *ibpA-msfGFP* reporter background (60-min L-ara treatment) led to the formation of foci, with ~48% of cells having three foci and ~20% having two or four foci (Fig. 5B). As a control, the empty pBAD plasmid was transferred to the *ibpA-msfGFP* reporter background, and the resulting strain was treated with L-ara. However, L-ara alone was not sufficient to cause foci formation (Fig. 5B). To demonstrate that functional TisB was needed for ATP depletion and foci formation, plasmid p0SD-*tisB-K12L* was applied for production of the TisB-K12L variant. TisB-K12L has central lysine 12 replaced with leucine, leading to attenuated TisB activity without affecting membrane localization (40). As expected, TisB-K12L did not cause major ATP depletion (Fig. 5A). More intriguingly, a reporter strain containing p0SD-*tisB-K12L* displayed mainly cells without foci (~83%) after 60 min of L-ara treatment (Fig. 5B). This control experiment demonstrated that production of a small membrane protein (TisB-K12L) is not sufficient to cause cytosolic protein aggregation, but rather that functional TisB toxin triggers the formation of protein aggregates, probably due to strong intracellular ATP depletion.

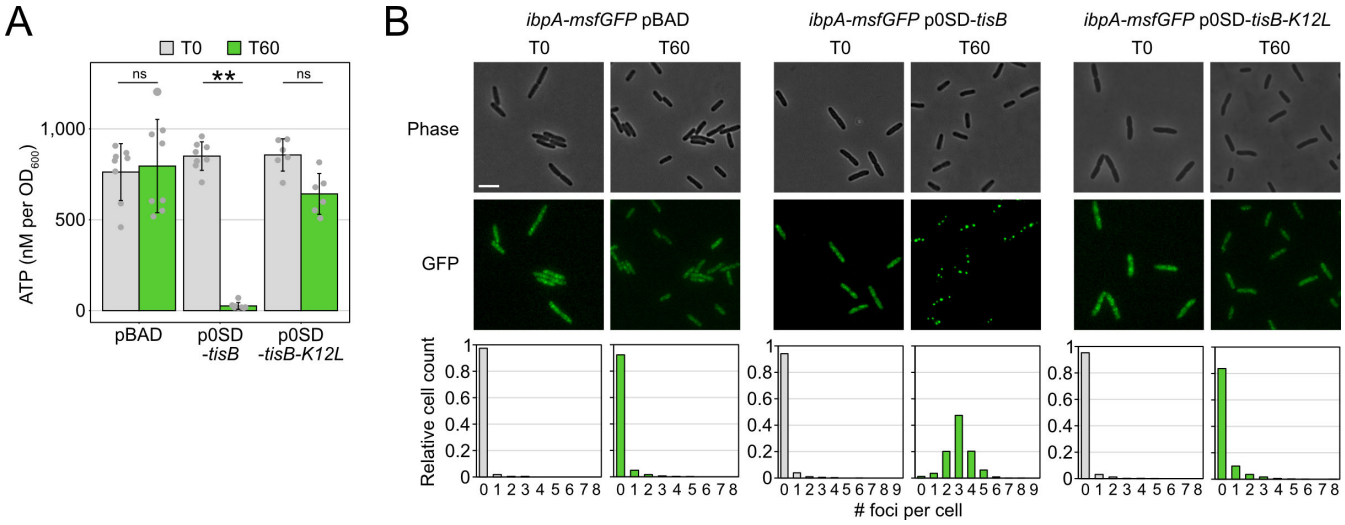

FIG 5 Expression of *tisB* causes cytoplasmic protein aggregation. (A) TisB-dependent ATP depletion. Wild-type MG1655, harboring either an empty pBAD plasmid, the p0SD-*tisB* plasmid, or the p0SD-*tisB-K12L* variant, was treated with L-ara (0.2%) during the exponential phase (OD_{600} ~0.4) for 60 min. A luciferase-based assay was applied to measure cellular ATP levels (nM per OD_{600}) before (T0) and after L-ara treatment (T60). Bars represent the mean of at least six biological replicates and error bars indicate the standard deviation. Dots show individual data points (pBAD: *n* = 8; p0SD-*tisB*: *n* = 8; p0SD-*tisB-K12L*: *n* = 6). ANOVA with post hoc Tukey HSD test was performed (**$P < 0.01$; ns: not significant). (B) TisB-dependent protein aggregation in the cytoplasm. Strain MG1655 *ibpA-msfGFP*, harboring an empty pBAD plasmid, the p0SD-*tisB* plasmid, or the p0SD-*tisB-K12L* variant, was treated with L-ara (0.2%) during exponential phase (T0; OD_{600} ~0.4) for 60 min (T60). Phase contrast images are displayed together with corresponding fluorescence images (GFP). White bars represent a length scale of 2 µm. Representative images from three biological replicates are shown. In the lower panel, msfGFP foci were quantified from three biological replicates. All images were evaluated using a U-Net neural network analysis and in-house image processing tools to automatically count msfGFP foci per cell. At least 507 cells were analyzed for each condition (pBAD T0: *n* = 507; pBAD T60: *n* = 3,019; p0SD-*tisB* T0: *n* = 730; p0SD-*tisB* T60: *n* = 1,474; p0SD-*tisB-K12L* T0: *n* = 1,405; p0SD-*tisB-K12L* T60: *n* = 1,896).

Ciprofloxacin provokes TisB-dependent protein aggregation

So far, we have shown that *tisB* expression from plasmid p0SD-*tisB* induces several stress-related genes, encoding—among others—the chaperones CpxP, Spy, and IbpB. Deletion of these genes delays the recovery of cells following TisB-mediated stress. Furthermore, we have observed strong ATP depletion and protein aggregation upon *tisB* expression from plasmid p0SD-*tisB*. While these experiments are helpful in appreciating the cellular consequences of *tisB* expression, they do not provide direct evidence for the consequences of *tisB* expression in wild-type cells. In wild-type cells, *tisB* transcription is strongly induced upon DNA damage through UV light or DNA-damaging agents, such as mitomycin C or ciprofloxacin (39, 41, 42, 66). When using the gyrase inhibitor ciprofloxacin (CIP), most TisB-dependent effects are observed only after approximately 3 hours of a high-dose treatment (31). We, therefore, treated wild-type MG1655 and a corresponding *tisB* deletion mutant with CIP at a high concentration (10 µg/mL), which was 1,000× higher than the minimum inhibitory concentration (MIC). Intracellular ATP concentrations were determined over 6 hours. In wild-type cultures, a ~1.7-fold drop of ATP was only observed after four hours of CIP, while ATP concentrations even significantly increased in the *tisB* deletion mutant (Fig. 6A). It should be noted that the drop of ATP in CIP-treated wild-type cultures was not comparable to the drastic ATP depletion observed upon *tisB* expression from plasmid p0SD-*tisB* (Fig. 5A). However, ~66% of wild-type cells displayed one or two IbpA-msfGFP foci after 6 hours of CIP, indicating protein aggregation, which was not observed in the *tisB* deletion background (Fig. 6B). This led us to conclude (i) that TisB-dependent protein aggregation occurs in wild-type cells after prolonged DNA-damage stress and (ii) that ATP depletion is likely not the determining factor for TisB-dependent protein aggregation upon CIP treatment.

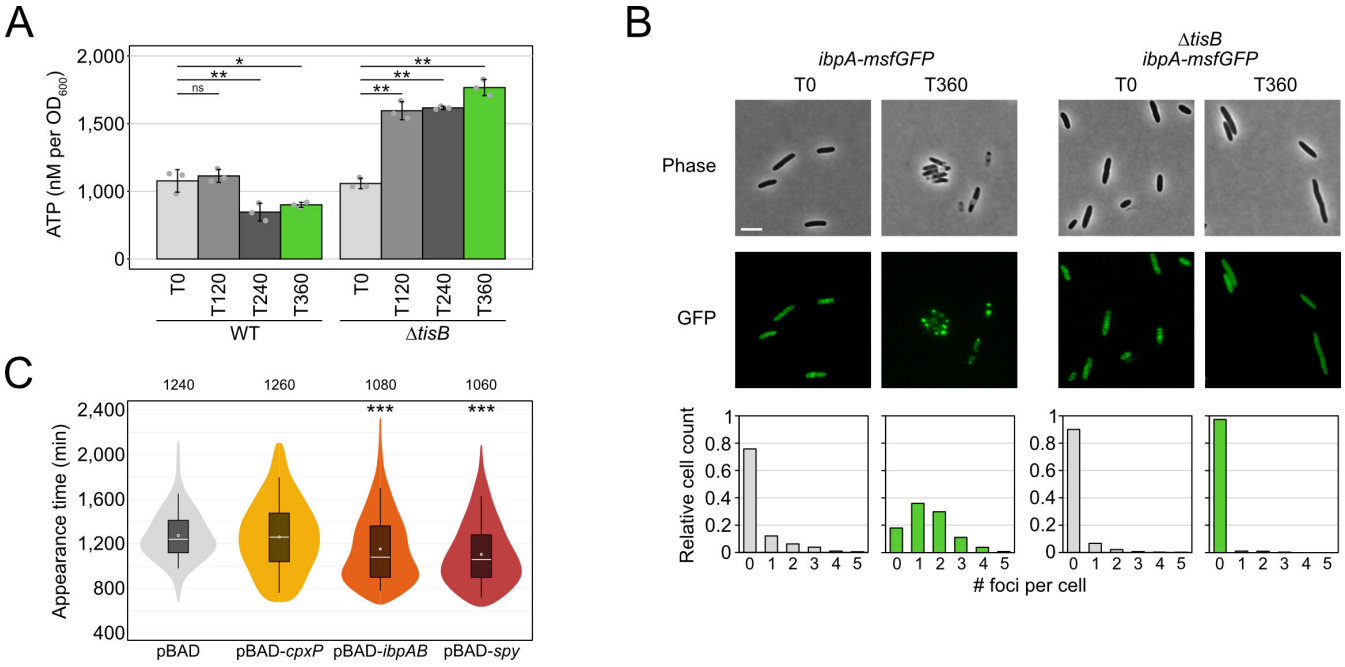

FIG 6 Analysis of TisB-dependent protein aggregates in wild-type cultures upon CIP treatment. (A) WT MG1655 and a *tisB* deletion mutant were treated with CIP (10 µg/mL; 1,000× MIC) during the exponential phase (OD_{600} ~0.4) for 360 min. A luciferase-based assay was applied to measure cellular ATP levels (nM per OD_{600}) before (T0) and after 120 min (T120), 240 min (T240), and 360 min (T360) of L-ara treatment. Bars represent the mean of three biological replicates, with two technical replicates each, and error bars indicate the standard deviation. Dots show individual data points. ANOVA with post hoc Tukey HSD test was performed (*P < 0.05, **P < 0.01, ns: not significant). (B) Strain MG1655 *ibpA-msfGFP* and Δ*tisB ibpA-msfGFP* were treated with CIP (10 µg/mL; 1,000× MIC) during exponential phase (T0; OD_{600} ~0.4) for 360 min (T360). Phase contrast images are displayed together with corresponding fluorescence images (GFP). White bars represent a length scale of 2 µm. Representative images from three biological replicates are shown. In the lower panel, msfGFP foci were quantified from three biological replicates. All images were evaluated using a U-Net neural network analysis and in-house image processing tools to automatically count msfGFP foci per cell. At least 577 cells were analyzed for each condition (*ibpA-msfGFP* T0: n = 766; *ibpA-msfGFP* T360: n = 577; Δ*tisB ibpA-msfGFP* T0: n = 1,621; Δ*tisB ibpA-msfGFP* T360: n = 901). (C) Influence of chaperone overexpression on recovery. Wild-type MG1655, harboring pBAD-*cpxP*, pBAD-*ibpAB*, pBAD-*spy,* or an empty pBAD plasmid, was pre-treated with the inducer L-ara (0.2%) for 30 min prior to the addition of CIP (10 µg/mL; 1,000× MIC) during exponential phase (OD_{600} ~0.4) for 6 hours. ScanLag was applied to determine the colony appearance time after CIP treatment. Colony appearance times are illustrated as violin box plots. Colonies from at least six biological replicates were combined (pBAD: n = 471; pBAD-*cpxP*: n = 266; pBAD-*ibpAB*: n = 479; pBAD-*cpxP*: n = 373). The white dot indicates the mean. The respective median appearance time (white bar) is shown on top of each plot. The chaperone overexpression strains were compared to the empty pBAD plasmid using a pairwise Wilcoxon rank-sum test (***P < 0.0001).

Since single deletions of the chaperone genes *cpxP*, *ibpB*, and *spy* extended the recovery time following plasmid-based *tisB* expression (Fig. 4B), we tested whether the corresponding gene deletions would also affect the recovery time of *E. coli* MG1655 following treatment with CIP. However, neither single nor double gene deletions affected recovery (data not shown). However, when expression of the *ibpAB* operon or the *spy* gene was induced from a plasmid 30 min prior to CIP treatment, the appearance time in ScanLag experiments was reduced by 160–180 min (Fig. 6C), indicating that increased IbpAB and Spy levels supported the recovery after CIP-induced stress.

Proteome analysis of aggregates

To further analyze TisB-dependent protein aggregates, wild-type cultures were treated with CIP, and aggregate-containing pellet fractions (PF) were separated from supernatants (SN) according to an established procedure (63) (Fig. 7A). The *tisB* deletion mutant was analyzed in parallel as a control for TisB-independent effects. The approach was initially validated by western blot analysis using the *ibpA-msfGFP* reporter background and detection of IbpA-msfGFP, confirming that the procedure was suitable to specifically enrich protein aggregates in wild-type PF samples (Fig. 7B). We then

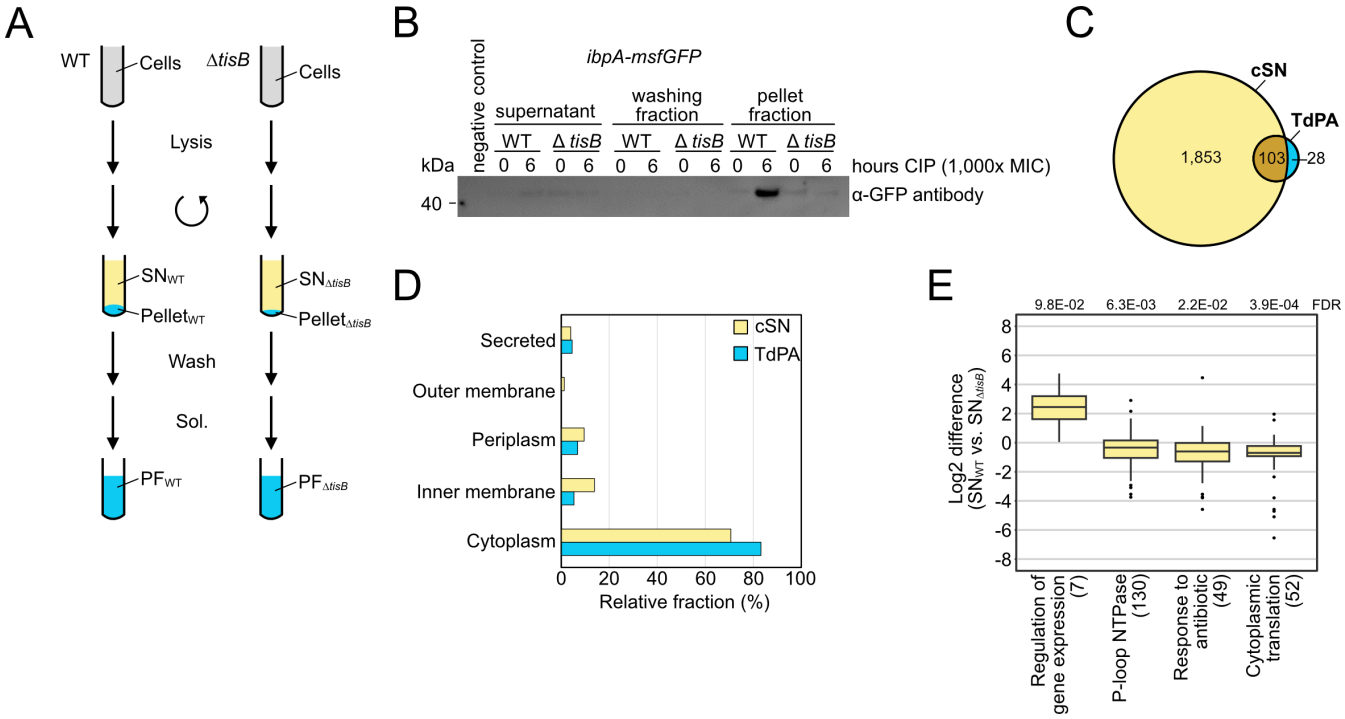

FIG 7 Proteome analysis of aggregates. (A) Schematic representation of the protein aggregate purification procedure. WT MG1655 and a *tisB* deletion mutant (Δ*tisB*) were treated with CIP (10 µg/mL; 1,000× MIC) during the exponential phase (OD_{600} ~0.4) for 6 hours. After cell lysis and centrifugation, SNs were collected for LC-MS analysis. The pellet fractions were washed three times and solubilized (Sol.) to receive pellet fractions (PF) for LC-MS analysis. (B) Western blot validation of protein aggregate purification. WT MG1655 *ibpA-msfGFP* and Δ*tisB ibpA-msfGFP* were treated with CIP (10 µg/mL; 1,000× MIC) during exponential phase (OD_{600} of ~0.4) and samples were collected at the indicated time points as described in Materials and Methods. A western blot was performed to detect IbpA-msfGFP using an α-GFP antibody. (C) Euler diagram of proteins identified by LC-MS. All proteins that were identified in at least two biological replicates of either wild-type or Δ*tisB* supernatant samples were combined (combined supernatant; cSN) and used as a reference data set. All proteins that were exclusively present or enriched in wild-type pellet fractions in comparison to Δ*tisB* were defined as TisB-dependent protein aggregates (TdPA). (D) Protein localization was predicted using LocTree3. The relative fractions of different protein localizations are shown for the combined supernatant (cSN) and TisB-dependent protein aggregates (TdPA). (E) 1D annotation enrichment results of differentially abundant proteins in the SN_{WT} versus $SN_{\Delta tisB}$ (number of enriched terms in brackets; Benjamini-Hochberg FDR provided on top).

performed the experiment in wild-type MG1655 and the corresponding *tisB* deletion mutant and analyzed SN and PF samples by liquid chromatography-mass spectrometry (LC-MS). The combined supernatant (cSN) of wild-type and Δ*tisB* cultures comprised 1,956 proteins in total, which was used as a reference data set (Fig. 7C). Analysis of the PF samples identified 29 proteins that were significantly enriched in wild-type PF samples in comparison to Δ*tisB* (log_2 fold change > 1 and Welch's *t*-test with Benjamini-Hochberg FDR < 0.05; Data Set S2). The sHSPs IbpA (log_2 fold change of 5.6) and IbpB (log_2 fold change of 3.2) were among the proteins with the highest enrichment factor, which confirmed a successful purification of protein aggregates in wild-type PF samples. Furthermore, we identified 102 proteins that were only present in wild-type PF samples but absent from Δ*tisB* PF samples (Data Set S2). The combination of both groups (131 proteins in total) was defined as "TisB-dependent protein aggregates" (TdPA; Fig. 7C). There was no intriguing difference between TdPA and cSN proteins concerning molecular weight or isoelectric point (Fig. S8). We speculated that TisB interferes with the export of outer membrane proteins (OMPs) and/or membrane insertion of inner membrane proteins (IMPs) (67). However, there was no enrichment of OMPs or IMPs in the TdPA data set (Fig. 7D). In support of this finding, *in vitro* experiments showed that inner membrane vesicles from CIP-treated wild-type cultures were not compromised in the transport of the outer membrane protein OmpA (Fig. S8). Finally, a STRING database search (68) revealed that no specific functional protein groups were enriched within

the TdPA data set, despite the occurrence of seven proteins that are encoded in the *E. coli* K-12 cryptic prophages, including integrases IntA, IntF, and IntE, excisionase XisE, repressor YmfK, cell division inhibitor YmfM, and transcriptional regulator YmfT (Fig. S8). In summary, we were not able to identify striking features of the TdPA proteins.

To learn more about the CIP-induced and TisB-dependent stress response, we compared SN samples by label-free quantification, revealing four functional categories that showed either increased or decreased protein abundance in the wild type as compared to the Δ*tisB* mutant (Fig. 7E). Among the category with increased protein abundance ("regulation of gene expression"), we found several cold-shock proteins (CspA, CspC, CspD, and CspE). The remaining categories contained proteins with decreased abundance, including 130 P-loop NTPases, 49 proteins with a potential role in response to antibiotic, and 52 ribosomal subunit proteins ("cytoplasmic translation"). The decreased abundance of ATP-utilizing NTPases and ribosomal subunit proteins suggests that TisB-producing cells reduce energy-consuming core processes, such as replication and translation, upon CIP-induced stress.

Protein aggregates determine the dormancy duration of persister cells after ciprofloxacin treatment

We asked the question of whether protein aggregation affects the state of persister cells upon treatment with CIP. Since the *tisB* deletion mutant does not form protein aggregates at the regular incubation temperature of 37°C, we applied heat stress at 46°C to induce aggregation (Fig. 8A). After 6 hours of CIP treatment at 37°C, survival was reduced by ~20-fold in Δ*tisB* as compared to the wild type (Fig. 8B). This is in agreement with previous results showing that TisB is an important factor for persister cell survival upon CIP treatment (33, 39). At 46°C, however, survival was comparable between both strains (Fig. 8B). A transcriptional *ibpB-syfp2* fusion confirmed that both strains showed similar induction of the heat shock response (Fig. S9). When applying the ScanLag method for cultures that were treated with CIP at 37°C, we observed that colonies of the Δ*tisB* mutant appeared on average 300 min earlier than wild-type colonies (Fig. 8C), indicating a reduced dormancy duration of Δ*tisB* cells, probably because aggregates were absent.

(Continued on next page)

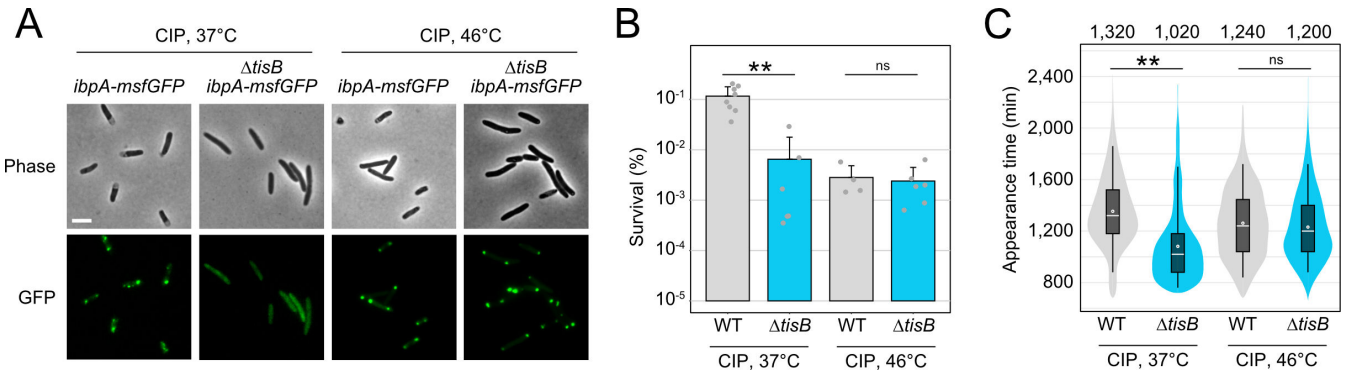

FIG 8 Heat-induced protein aggregates affect recovery from CIP. (A) Strain MG1655 *ibpA-msfGFP* and Δ*tisB ibpA-msfGFP* were treated with CIP (10 µg/mL; 1,000× MIC) during the exponential phase (OD_{600} ~0.4) for 6 hours at 37°C or 46°C. Phase contrast images are displayed together with corresponding fluorescence images (GFP). White bars represent a length scale of 2 µm. (B) WT MG1655 and a *tisB* deletion mutant were treated with ciprofloxacin (10 µg/mL; 1,000× MIC) during the exponential phase (OD_{600} ~0.4) for 6 hours at 37°C or 46°C. Pre- and post-treatment samples were used to determine relative CFU (%). Bars represent the mean of at least four biological replicates and error bars indicate the standard deviation. Dots show individual data points (WT 37°C: n = 8; Δ*tisB* 37°C: n = 6; WT 46°C: n = 4; Δ*tisB* 46°C: n = 6). ANOVA with post-hoc Tukey HSD was performed (**P < 0.01, ns: not significant). (C) WT MG1655 and a *tisB* deletion mutant were treated with ciprofloxacin (10 µg/mL; 1,000×MIC) during exponential phase (OD_{600} ~0.4) for 6 hours at 37°C or 46°C. ScanLag was applied to determine the colony appearance time after CIP treatment. Colony appearance times are illustrated as violin box plots. Colonies from at least three biological replicates were combined (WT 37°C: n = 1,431; Δ*tisB* 37°C: n = 272; WT 46°C: n = 476; Δ*tisB* 46°C: n = 1,026). The white dot indicates the mean. The respective median appearance time (white bar) is shown on top of each plot. The Δ*tisB* mutant was compared to the corresponding wild type MG1655 using a pairwise Wilcoxon rank-sum test (**P < 0.0001, ns: not significant).

When CIP was applied at 46°C, colony appearance times were comparable, suggesting that heat-induced protein aggregation has the potential to delay the recovery of Δ*tisB* persisters.

DISCUSSION

Dormancy is an efficient strategy to survive harmful situations. It is, therefore, not surprising that microorganisms have evolved different mechanisms to induce dormancy. A hallmark of toxins from chromosomal TA systems is their ability to halt cell growth, induce dormancy, and eventually promote persistence, especially when toxins are expressed from plasmids (32, 33, 39, 69–72). However, strong toxin expression from plasmids does not necessarily reflect the natural situation, potentially limiting the validity of the obtained effects. Here, we introduce an inducible system for moderate *tisB* expression that avoids toxic effects but retains the dormancy-promoting feature. Instead of manipulating transcription initiation (38, 51), we manipulated translation initiation by introducing an artificial SD-free 5′ UTR to the *tisB* gene on the pBAD expression plasmid. In *E. coli*, native transcripts without canonical SD sequences are not necessarily compromised in translation efficiency, suggesting that an SD sequence is not mandatory for efficient translation initiation (73). Here, we observed that the artificial SD-free 5′ UTR reduced TisB protein levels by ~10-fold in comparison to the native *tisB* 5′ UTR. We suggest that the SD-free 5′ UTR used in this study is a valuable genetic element that enables moderate expression of toxic genes, which may be especially useful when the resulting proteins have the potential to cause cell lysis or DNA damage (74–76). However, in the case of *tisB*, we observed inconsistent expression levels after extended cultivation, which might limit the use of the system to short-term experiments. Whether this represents a gene-specific feature requires further investigation.

The moderate *tisB* expression system was applied to reveal the response to TisB-mediated stress in *E. coli*. Our RNA-seq data are in good agreement with an earlier transcriptome study of a *tisB* overexpression strain (47). When comparing both analyses, the most prominent upregulated features are (i) the oxidative stress regulator gene *soxS*, (ii) the *ibpAB* operon, and (iii) CpxR-dependent genes, such as the chaperone genes *spy* and *cpxP*. It has been demonstrated that TisB provokes the formation of the reactive oxygen species superoxide, leading to strong *soxS* induction (40). The ability to detoxify superoxide by the superoxide dismutases SodA and SodB is important for recovery from TisB-induced dormancy (40). Here, we observed a similar pattern: the absence of stress-related proteins (e.g., chaperones IbpB, CpxP, or Spy) delayed the recovery from TisB-induced dormancy. We conclude that the TisB-dependent stress response mainly promotes the recovery process by repairing damages and restoring cellular integrity, as we have already speculated earlier (49). Recovery from TisB-induced dormancy would not only demand factors that cope with the cellular stress but also mechanistic means to remove the toxin and repolarize the inner membrane. In the case of membrane toxin HokB in *E. coli*, it has been observed that HokB pores are disassembled and targeted for degradation by DegQ protease, followed by membrane repolarization mediated by the electron transport chain (77). Whether similar mechanisms initiate the recovery from TisB-induced dormancy is currently unknown.

Chaperones are universal to all living cells and play important roles in protein quality control and disaggregation of protein aggregates (78, 79). The sHSPs IbpA and IbpB are chaperones that initiate the disaggregation process in the cytoplasm. Further components with a pivotal role in disaggregation and ATP-dependent protein re-folding are the DnaK-DnaJ-GrpE chaperone system, the ClpB disaggregase, chaperonins GroES and GroEL, and the ATP-dependent protease HslUV. Besides *ibpAB*, both our RNA-seq approach and proteome analysis revealed TisB-dependent upregulation of *clpB*, *groL,* and *hslU*, albeit they did not match our cutoff criteria. The prevalence of chaperone genes led to the hypothesis that *tisB* expression provokes protein aggregation, and indeed, cytosolic aggregates were observed upon *tisB* expression using an established fluorescent reporter system. Besides cytosolic chaperones, our data highlight

the functional importance of the periplasmic chaperones Spy and CpxP, both belonging to the CpxR regulon. While Spy is an ATP-independent chaperone that protects OMPs from folding stress (80, 81), CpxP might have a dual function by both regulating the Cpx response and acting as a chaperone (57, 82). Although not further investigated here, we suggest that *tisB* expression leads to protein folding stress in the cell envelope, thereby activating the Cpx response.

The membrane toxin TisB is well studied with regard to its inducing condition (i.e., SOS response following DNA damage) (33, 39, 42). TisB-dependent effects can, therefore, be revealed upon treatment with the DNA-damaging antibiotic CIP (31). Antibiotics have already been associated with an increased abundance of heat shock proteins and chaperones, as, for example, observed in *Pseudomonas aeruginosa* treated with the aminoglycoside tobramycin (83), *Streptococcus pneumoniae* treated with the β-lactam penicillin (84), or *Acinetobacter baumannii* treated with different classes of antibiotics (85). In *E. coli*, the deletion of heat shock proteins and chaperones resulted in reduced survival upon treatment with levofloxacin (86), a fluoroquinolone (FQ) antibiotic that is functionally related to CIP. The authors assumed that FQ antibiotics induce the formation of cytosolic protein aggregates, which need to be disassembled by heat shock proteins and chaperones (86). Intriguingly, we can demonstrate that protein aggregation occurs upon treatment with CIP and that this process depends on TisB, suggesting that TisB is the foremost factor for protein aggregation in response to FQ-induced DNA damage. The question remains how a membrane toxin provokes aggregation. Hypothetically, TisB accumulates in the cytoplasm and initiates a nucleation process that leads to aggregate formation (87). However, cellular fractionation experiments combined with western blot analysis indicate that TisB does not accumulate in the cytoplasm but rather completely localizes to the membrane (our unpublished results). Furthermore, we show here that the production of the attenuated toxin TisB-K12L does not trigger aggregation. We conclude that aggregation is a downstream effect of TisB and its function as a pore-forming toxin. Strong ATP depletion might be the crucial factor that drives TisB-dependent protein aggregation when *tisB* is expressed from the p0SD-*tisB* systems (62, 63). However, strong ATP depletion was not observed in CIP-treated wild-type cells and therefore fails to convincingly explain the CIP-induced protein aggregation. The primary action of TisB is the breakdown of the proton motive force (39), which is similar to the action of protonophores and leads to disturbance of pH homeostasis and acidification of the cytoplasm (88–90). Potentially, the drop in intracellular pH initiates the aggregation process (91), but this needs further investigation. Interestingly, it was observed only recently that TisB is the major factor for cytoplasmic condensation upon treatment with the DNA-damaging antibiotic ofloxacin (90). Whether cytoplasmic condensation and protein aggregation are intertwined processes remains an exciting issue for future studies.

Analysis of TisB-dependent protein aggregates revealed the enrichment of proteins from cryptic prophages, and it remains an open question whether this is coincidental or has a biological meaning. *E. coli* K-12 harbors nine cryptic prophages, and—albeit their functions remain largely unknown—it has been observed that they contribute to survival under antibiotic stress, including the DNA-damaging quinolone nalidixic acid (92). Potentially, the prophage proteins contribute to the aggregation process, which, in turn, affects antibiotic tolerance, but this needs further investigation.

Our data indicate that the occurrence of protein aggregates correlates well with an increased dormancy duration, which is in accordance with previous observations (62, 63). The dormancy duration might also ultimately affect persister levels. The wild-type had ~20-fold more persister cells than the *tisB* deletion mutant when treated with CIP at 37°C, corroborating former results (33, 39), but persister levels were comparable at 46°C. This apparent discrepancy can be solved when persister levels are seen as a dynamic measure that is mainly determined by the dormancy duration or, in other words, by the "kinetics of awakening" (93). At 37°C, the *tisB* deletion strain does not form protein aggregates, wakes up early, is killed by CIP and, hence, has a reduced persister level as

compared to the wild type. At 46°C, however, both strains form aggregates and wake up with the same kinetics, resulting in comparable persister levels. These considerations may also help to solve a recurrent discrepancy in the literature regarding TisB-dependent persistence. When *E. coli* is treated with CIP while growing in complex media, such as LB or Mueller-Hinton broth, a *tisB* deletion strain scores fewer persister cells than a wild type (33, 39). By contrast, when a MOPS-based minimal medium and ofloxacin are applied, a *tisB* deletion strain and a wild type have similar persister levels (90, 94). We assume that in MOPS medium wake-up kinetics are comparable between both strains, resulting in similar killing kinetics and, hence, persister levels. However, we cannot exclude that the antibiotic of choice (CIP versus ofloxacin) may have contributed to the conflicting results obtained in different laboratories. In conclusion, we propose that the primary function of the membrane toxin TisB is the establishment of a dormant state through energy depletion, but that secondary effects and environmental conditions determine the dormancy duration, which, in turn, affects long-term survival.

MATERIALS AND METHODS

Growth conditions

E. coli strains were grown in lysogeny broth (LB) medium at 37°C and 180 rpm. If temperature-sensitive plasmids were present, strains were grown at 30°C and 180 rpm. Pre-cultures were cultivated in the presence of antibiotics if applicable (50 µg/mL kanamycin, 15 µg/mL chloramphenicol, 200 µg/mL ampicillin, and 6 µg/mL tetracycline). Pre-cultures were diluted 100-fold into fresh LB medium and grown until the exponential phase was reached. Growth curves were recorded in 30-min time intervals with a cell density meter model 40 (Fisher Scientific).

Construction of strains and plasmids

E. coli strains used in this study are derivatives of K-12 wild-type MG1655 and are listed in Table S1. Chromosomal deletion or transcriptional fusion mutants were constructed using the λ red methodology (95). A selection marker (*cat* or *kan* gene) was amplified via PCR using primers with specific 40 bp overhangs, matching the desired deletion locus. An *E. coli* MG1655 strain, that provides the heat-inducible λ red genes on plasmid pSIM5-tet (96), was grown at 30°C in the presence of tetracycline (3 µg/mL) until an OD_{600} of ~0.4 was reached. After a 15-min heat shock at 42°C, electrocompetent cells were prepared and PCR products were transformed via electroporation. Clones were selected on LB agar plates containing the appropriate antibiotic (12.5 µg/mL chloramphenicol or 50 µg/µL kanamycin), and gene deletions were subsequently verified by colony PCR. After two incubations at 42°C, loss of the heat-sensitive plasmid pSIM5-tet was verified by tetracycline sensitivity. If necessary, deletion constructs were transduced into new strain backgrounds using P1 phages according to standard protocols.

Expression plasmid p0SD-*tisB* was generated by AQUA cloning (97). The *tisB* insert was amplified by PCR using primer pair AQ-0ATG-2-f/NES-rev and plasmid p+42-*tisB* as a template. Primer AQ-0ATG-2-f provides both a 20 bp artificial 5′ UTR (lacking a Shine-Dalgarno sequence) and a 20 bp overhang for AQUA cloning. The pBAD backbone was amplified by PCR using primer pair AQ-topo-f/AQ-topo-rev to generate matching overhangs for the *tisB* insert. Purified amplification products were mixed in a final volume of 10 µL, applying a molecular ratio of 7:1 (insert to backbone; 100 ng backbone). Mixtures were incubated at 25°C for 1 hour. Afterward, mixtures were transformed into chemically competent MG1655 cells and clones were selected on LB agar containing ampicillin (200 µg/mL). In a similar way, plasmid p0SD-*3xFLAG-tisB* was generated with primer pair AQ-0ATG-3x-f/NES-rev using plasmid p+42–*3xFLAG-tisB* as a template for amplification of the *3×FLAG-tisB* insert. Plasmid p0SD-*tisB-K12L* was generated by site-directed mutagenesis PCR using primer pair K12L-for/K12L-rev and plasmid p0SD-*tisB* as template. After PCR, parental plasmids were digested with DpnI (Thermo Fisher Scientific), and the linear PCR product was transformed into chemically

competent MG1655 cells. Clones were selected on LB agar containing ampicillin (200 µg/mL). For the generation of *cpxP*, *ibpAB*, and *spy* overexpression plasmids, the corresponding genes were amplified via PCR using primers containing BbsI recognition sites for the generation of specific overhangs. PCR products were cloned into plasmid pSL0002 using Golen Gate cloning as described elsewhere (98). For the generation of plasmid p0SD-*syfp2*, the pBAD backbone (37) and the *syfp2* open reading frame were amplified via PCR with primers introducing recognition sites for EcoRI and HindIII, followed by restriction and ligation. The forward primer for *syfp2* contained a sequence for the 20 bp artificial 5′ UTR. The ligation product was transformed into electrocompetent *E. coli* MG1655 cells. Clones were selected on LB agar containing ampicillin (200 µg/mL). All plasmids were verified by Sanger sequencing (Microsynth SeqLab, Göttingen, Germany) and are listed in Table S2. Primers used for cloning procedures are listed in Table S3.

Determination of relative colony counts and persister levels

Exponential-phase cultures (OD_{600} ~ 0.4) were treated with L-ara (0.2%) for 1 hour or with CIP (10 µg/µL; 1,000× MIC) for 6 hours at 37°C and 180 rpm. Pre- and post-treatment samples were serially diluted and plated on LB agar plates. In the case of L-ara treatment, cells were diluted with NaCl (0.9%). In the case of CIP treatment, cells were washed two times and diluted with 20 mM $MgSO_4$. Colonies were counted after ~20 hours (pre-treatment) or ~40 hours (post-treatment). Colony counts were used to determine CFU per milliliter. The ratio between treated and untreated samples represents either the relative CFU count (L-ara) or persister level (CIP). *P*-values were calculated using an ANOVA with a post hoc Tukey HSD test in R statistical language (https://www.r-project.org/).

Analysis of colony growth

Colony growth was analyzed using the ScanLag method (55). Agar plates from L-ara or CIP treatments (see "Determination of relative CFU counts and persister levels") were covered with black felt, placed on scanners, and incubated at 37°C. Epson Perfection V39 scanners were used to record a time series of images controlled by the ScanningManager application. Images (TIFF files) were taken every 20 min for a total period of 40 hours. Image processing was performed using MatLab (MathWorks) with functions PreparePictures, setMaskApp, TimeLapse, and ScanLagApp (54). After image processing, the appearance and growth times were extracted. The appearance time is defined by a colony size of 10 pixels, whereas the growth time is defined as the time that is needed to cause a colony size increase from 80 to 160 pixels. Growth data were used to create violin box plots with Power BI Desktop (Microsoft). *P*-values were calculated using a pairwise Wilcoxon rank-sum test in R statistical language (https://www.r-project.org/).

Membrane depolarization measurements

Exponential-phase cultures (OD_{600} ~0.4) were treated with 0.2% L-ara for 1 hour at 37°C and 180 rpm. Samples were withdrawn before and after the addition of L-ara and adjusted to an OD_{600} of 0.5. $DiBAC_4(3)$ (Sigma-Aldrich) was added at a final concentration of 1 µg/mL, followed by incubation for 20 min in the dark at room temperature. $DiBAC_4(3)$ fluorescence was measured via flow cytometry using a FACSCalibur (BD) and the FL1-H detector (ex: 488 ± 10 nm, em: 530 ± 30 nm). CellQuest Pro 4.0.2 (BD) was applied as an operating system. Data were analyzed with FlowJo v.10 (FlowJo LLC). Cell counts were normalized to ~10,000 events by application of the DownSample plugin.

ATP measurements

Cultures were grown to exponential phase (OD_{600} ~0.4) and treated with L-ara (0.2%) for 1 hour or with CIP (10 µg/µL; 1,000× MIC) for up to 6 hours. Samples (1 mL) were withdrawn before and after treatment. Cell pellets were collected by centrifugation (13,000 rpm, 3 min) and supernatants were discarded. Cells were washed with 1 mL NaCl (0.9%) and resuspended in 1 mL LB medium. 100 µL of samples was mixed

with 100 µL BacTiter-Glo reagent (Promega) and incubated for 5 min in the dark. The luminescence was measured using an Infinite M Nano$^+$ microplate reader (Tecan). Values were transformed to nM, using the slope formula of an ATP calibration curve, and normalized to the OD_{600}. *P*-values were calculated using an ANOVA with a post-hoc Tukey HSD test in R statistical language (https://www.r-project.org/).

Fluorescence microscopy

Cultures were grown to exponential phase (OD_{600} ~0.4) and treated with L-ara (0.2%) for 1 hour or with CIP (10 µg/µL; 1,000× MIC) for 6 hours at 37°C or 46°C. Samples before and after treatment were transferred onto agarose pads (1% agarose in 1× PBS) on top of a microscopy slide with a cover slip on top of the cells. Images were recorded with a Leica DMI 6000 B inverse microscope (Leica Camera AG) using an HCX PL APO 100×/1.4 phase contrast objective, a pco.edge sCMOS camera (PCO AG), and software VisiView version 4.3.0 (Visitron Systems GmbH). For fluorescence images (GFP), a custom filter set (T495lpxr, EX470/40 m; EM525/50; Chroma Technology) was used. The exposure time was set to 50 ms with a binning of 2 and an offset of 0.0. Images were saved as TIFF and further processed with the open-source software ImageJ version 1.53 k.

Automated focus analysis

For U-Net training and segmentation, phase contrast images of *E. coli* cells were used. The software used was the U-Net plugin for ImageJ, available from the website of the Computer Vision Group at the University of Freiburg (65). For training, 906 cells in eight images were annotated. To enhance segmentation quality and facilitate the separation of cell aggregates into individual cells, one label was used for the circumference of the cells and one for their inside. A training with 2,000 iterations and a learning rate of 1E−4 yielded segmentations that were very close to the training annotation. With post-processing using a custom Wolfram Mathematica script, the segmentations were further refined and crooked, very small, very large features or cells at the image border were excluded. Visual inspection of all segmentations confirmed that the vast majority of cells were properly identified. The extracted cell shapes were used as masks for the GFP image channel. Spatial filtering, peak finding, and thresholding yielded the foci.

Preparation of RNA-sequencing samples

Exponential-phase cultures (OD_{600} ~ 0.4) of strain MG1655 p0SD-*tisB* were treated with 0,2% L-ara to induce *tisB* expression for 30 min. Samples from biological triplicates were withdrawn before (samples "Exp") and after L-ara treatment (samples "T30") and immediately inactivated by adding 200 µL stop solution (95% ethanol, 5% phenol) to 1 mL cell culture on ice. Total RNA was isolated according to the hot acid-phenol method as described (41). DNA was removed using the TURBO DNA-*free* kit (Invitrogen) according to the "rigorous treatment" instructions. The final clean-up was performed using phenol/chloroform/isoamyl alcohol (25:24:1) mixed with the sample in a 1:1 ratio, followed by chloroform treatment and precipitation as before. RNA quality was assessed on an 8% polyacrylamide gel containing 1× TBE and 7 M urea. Aliquots of approximately 3.5 µg of total RNA were prepared and stored at −80°C until further analysis.

RNA-sequencing and data analysis

RNA-sequencing was performed by vertis Biotechnologie AG. For cDNA synthesis, all RNA samples were first fragmented using ultrasound (4 pulses of 30 seconds, each at 4°C). Then, an oligonucleotide adapter was ligated to the 3′ end of the RNA molecules. First-strand cDNA synthesis was performed using M-MLV reverse transcriptase and the 3′ adapter as a primer. The first-strand cDNA was purified and the 5′ Illumina TruSeq sequencing adapter was ligated to the 3′ end of the antisense cDNA. The resulting cDNA was PCR-amplified to about 10–20 ng/µL using a high-fidelity DNA polymerase for 12 cycles. The TruSeq barcode sequences, which are part of the 5′ and 3′ TruSeq

sequencing adapters, were used. The cDNA was purified using the Agencourt AMPure XP kit (Beckman Coulter Genomics) and analyzed by capillary electrophoresis. For Illumina NextSeq sequencing, the samples were pooled in approximately equimolar amounts. The cDNA pool in the size range of 200–550 bp was eluted from a preparative agarose gel. An aliquot of the size-fractionated pool was analyzed by capillary electrophoresis. The cDNA pool was single-read sequenced on an Illumina NextSeq 500 system using 75 bp read length.

Quality and adapter trimming was performed with Trim Galore (Version 0.6.5) (https://github.com/FelixKrueger/TrimGalore) with Cutadapt Version 2.7 (http://dx.doi.org/10.14806/ej.17.1.200) using the parameters "--quality 20 --length 20" and default adapter detection and trimming. MultiQC (Version 1.8) (99) and FastQC (Version 0.11.8) (http://www.bioinformatics.babraham.ac.uk/projects/fastqc/) were used for quality control. The preprocessed reads were aligned with Bowtie2 (Version 2.3.5) (100) using the '--mm" and "--very-sensitive" settings and GCF_000005845.2 (NCBI; downloaded 25.11.2019) as a reference genome. For post-processing of the alignments, gene counting and data analysis, Samtools (Version 1.9) (101), featureCounts (Version 1.6.4) (102), and DESeq2 (Version 1.26) (103) were applied, respectively. All bioinformatic calculations were performed using Curare (Version 0.1.1) (https://github.com/pblumenkamp/Curare) and R statistical language (https://www.r-project.org/). Processed RNA-seq data are available as Data Set S1 and have been deposited together with raw data files on the NCBI Gene Expression Omnibus (GEO) under the accession number GSE255764.

Northern blot analysis

Cultures were grown to exponential phase (OD_{600} ~0.4) and treated with L-ara (0.2%) for 30 min. Total RNA for northern blot analysis was isolated using the hot acid-phenol method as described (41). Northern blot analysis was performed with 5–10 µg of total RNA. The RNA was separated using 10% polyacrylamide gels containing 1× TBE and 7 M urea at 300 V for approximately 3 hours. The RNA was transferred to a RotiNylon plus membrane (Roth) by semi-dry electroblotting at 250 mA for 3 hours. After UV-crosslinking, the membrane was pre-hybridized using Church buffer (0.5 M phosphate buffer [pH 7.2], 1% [wt/vol] bovine serum albumin, 1 mM EDTA, 7% [wt/vol] SDS) at 42°C for 1 hour. Hybridization with probes for detection was performed overnight. Specific probes were generated by end-labeling of oligodeoxyribonucleotides (Table S3) using T4 Polynucleotide Kinase (New England Biolabs) and [γ-^{32}P]ATP (Hartmann Analytic). Membranes were washed (5× SSC, 0.01% SDS) and exposed to phosphorimaging screens (Bio-Rad). Screens were analyzed using a Molecular Imager FX and the Quantity One 1-D Analysis Software (Bio-Rad).

Quantitative reverse transcription-PCR

Cultures were grown to exponential phase (OD_{600} ~0.4) and treated with L-ara (0.2%) 30 min. Total RNA for quantitative reverse transcription PCR (qRT-PCR) was isolated using the NucleoSpin RNA Kit (Macherey-Nagel), including DNA digestion. RNA concentrations were measured using a spectrophotometer (NanoDrop 1000) and subsequently adjusted to a concentration of 5 ng/µL. For reverse transcription and amplification of gene-specific fragments, 10 µL of reaction mixtures was prepared with the Brilliant III Ultra-Fast SYBR Green qRT-PCR Master Mix (Agilent) in technical duplicates for each sample. Reaction mixtures contained 1 ng/µL of total RNA and 0.5 µM of each primer (Table S3). Reverse transcription and amplification were performed on a CFX Connect Real-Time System (Bio-Rad). Reverse transcription was carried out at 50°C for 10 min followed by 95°C for 3 min. For amplification, 45 cycles were applied at 95°C for 5 seconds, 56°C for 10 seconds and 72°C for 10 seconds (*tisB* gene), or at 95°C for 5 seconds and 60°C for 10 seconds (all remaining genes). Amplification curves were recorded with the CFX Maestro software (Bio-Rad). Cq values were used to calculate fold changes according to Pfaffl (104). The *hcaT* gene was used as a reference for normalization (41).

Western blot analysis

For the detection of 3×FLAG-TisB, strains were grown to the exponential phase. Samples were withdrawn in a defined volume (equivalent to an OD_{600} of 10) and centrifuged at 10,000 rpm and 4°C for 10 min. Cell pellets were resuspended in 50 µL SDS sample buffer (12% SDS, 6% β-mercaptoethanol, 30% glycerol, 0.05% Coomassie blue, 150 mM Tris/HCl, pH 7.0). For protein separation, a Tricine-SDS-PAGE was applied with 16% polyacrylamide (105). Samples were incubated at 95°C for 10 min before loading onto the gel. An initial voltage of 60 V was applied until samples entered the separation gel. Afterward, electrophoresis was carried out at 100 V for about 3 hours. Proteins were transferred onto a PVDF membrane by semi-dry electroblotting overnight at 0.4 mA/cm². Membranes were stained with Ponceau S and documented before blocking with 5% milk powder in 1× PBST (PBS + 0.1% Tween20) for 1 hour. For detection of 3×FLAG-TisB, membranes were incubated with an HRP-conjugated monoclonal IgG α-FLAG antibody (Sigma-Aldrich) in 3% BSA in PBST at room temperature for 90 min. Using the Lumi-Light Western Blotting Substrate (Roche), 3×FLAG-TisB was visualized and documented in a chemiluminescence imager (PeqLab) with the FusionCapt Advance software (Vilber Lourmat).

Purification of protein aggregates

Protein aggregates were purified according to a published protocol (63) with minor modifications. Strains were grown to the exponential phase (OD_{600} ~0.4) and treated with CIP (10 µg/mL; 1,000× MIC) for 6 hours. Cells (38 mL culture volume) were harvested and centrifuged at 4,000 × *g* and 4°C for 30 min. Cells were resuspended in 10 mL washing buffer I (300 mM NaCl, 5 mM β-mercaptoethanol, 1 mM EDTA, 50 mM HEPES, pH 7.5) and centrifuged as before. The cell pellet was dissolved in 10 mL lysis buffer [washing buffer I containing 1 µg/mL leupeptin and 0.1 mg/mL 4-(2-aminoethyl)benzenesulfonyl fluoride hydrochloride (AEBSF)]. Cells were lysed in three cycles with a cell homogenizer at 1,380 to 1,725 bar, followed by centrifugation at 11,000 × *g* and 4°C for 30 min to clear the lysates. SNs were stored at −80°C until LC-MS analysis. Pellets were resuspended in 2 mL washing buffer II (washing buffer I containing 0.8% Triton X-100 and 0.1% sodium deoxycholate) and centrifuged as before. The washing step was repeated two more times. After the final washing step, pellets were resuspended in 1 mL solubilization buffer (1% SDS, 1× SigmaFast Protease Inhibitor [Sigma-Aldrich], 50 mM HEPES, pH 8.0). Pellet fractions (PF) were stored at −80°C until LC-MS analysis.

LC-MS-based proteome analysis

Samples generated via the purification of protein aggregates, that is, lysate supernatants and the protein aggregate pellets, were processed following the SP3 protocol (106). For the lysate supernatants and protein aggregate samples, 50 µg of each was analyzed. Briefly, all samples (in triplicate) were resuspended in 75 µL of 100 mM ammonium bicarbonate (ABC) buffer (pH 7.4). Samples were reduced in the presence of tris(2-carboxyethyl)phosphine (5 mM) (1 hour, 56°C), before alkylation was performed with chloroacetamide (50 mM) (room temperature [RT] in the dark, 30 min). Beads (SpeedBeads Magnetic Carboxylate) were washed twice with Milli-Q water, and 100 µg of beads in 250 mM ABC buffer were added to each sample (final volume of 100 µL per sample). Precipitation of the proteins onto the beads was initiated via the addition of 100 µL of ethanol, the samples were gently shaken (5 min, 800 rpm) before a further 300 µL of ethanol was added and the samples were gently shaken (800 rpm) for an additional 20 min (final concentration of ca. 80% ethanol). The bead-associated precipitated proteins were pelleted by centrifugation (21,100 × *g*, 5 min, RT) with magnet-assisted isolation to assist aspiration of the solution. The beads were then washed twice with 80% ethanol, with centrifugation (21,100 × *g*, 5 min, RT) and magnet-assisted aspiration to remove all liquid. The samples were briefly sonicated in a sonication bath between washes to aid in the re-solubilization of the protein-associated beads. Following the final wash, the beads were suspended in 100 µL of 100 mM ABC buffer containing

trypsin (0.4 µg in total per sample, enzyme to protein ratio of 1:125), the samples were briefly sonicated to ensure no aggregation of the beads, then incubated overnight (37°C, shaking at 1,300 rpm). Following overnight digestion, the samples were centrifuged (21,100 × *g,* 5 min), before magnet-assisted collection of the peptide-containing supernatant was performed. The peptides were cleaned up via solid phase extraction (SPE) using Pierce C18 Tips 100 µL (as per the manufacturer's protocol). Following cleanup, the supernatants were dried down via vacuum centrifugation and stored at −20°C. On the day of MS analysis, peptides were resuspended in 20 µL of HPLC loading buffer (3% acetonitrile and 0.1% trifluoroacetic acid).

Chromatographic separation was performed on a Dionex U3000 Nano-HPLC system equipped with an Acclaim PepMap 100 C18 column (2 µm particle size, 75 µm × 500 mm) coupled online to a mass spectrometer. The eluents used were as follows: eluent A (0.05% formic acid) and eluent B (80% acetonitrile and 0.04% formic acid). The separation was performed over a programmed 120 min run. Initial chromatographic conditions were 4% eluent B for 4 min followed by linear gradients from 4% to 50% eluent B over 90 min, then 50% to 95% over 8 min, and 8 min at 95% eluent B. Following this, an inter-run equilibration of the column was performed (20 min at 4% eluent B). A 300 nL/min flow rate and 1 µL of sample were injected per run. Two wash runs (loading buffer injections) were performed between each sample. Data acquisition following separation was performed on a Q Exactive Plus mass spectrometer (Thermo Fisher Scientific). A full scan MS acquisition was performed (350–1,000 *m/z*, resolution 70,000) with the subsequent data-dependent MS/MS acquisition for the top 15 most intense ions via HCD activation at NCE 26 (resolution 17,500); an isolation window of 3 *m/z* was employed with apex trigger (3–15 s) and dynamic exclusion (30 s duration) enabled.

Bottom-up proteomic data analysis was performed using Proteome Discoverer (Ver. 3.0.1.27) (Thermo Fisher Scientific), and the Chimerys search algorithm. In addition, the Minora node was included to enable label-free quantification. Raw data files were searched against a protein FASTA database containing the complete UniProt *E. coli* (K-12 substrain MG1655) protein FASTA (accessed from UniProt 2023.04.11) plus the list of common laboratory contaminants (cRAP47). The searches were conducted with trypsin specificity, allowing a maximum of two missed cleavages. Strict parsimony criteria were applied with high stringency at both the protein and peptide levels (protein level false discovery rate [FDR] < 1%), and at least one high unique confidence peptide (PSM level FDR < 1%). Statistical assessment of the data was performed using the Perseus software package (Ver. 2.0.10.0). The Welch's *t*-test was performed with a minimum of two valid quantification values required for each protein in both groups, and Benjamini-Hochberg FDR calculation was performed at both medium (FDR < 5%) and high (FDR < 1%) cut-off levels. In addition, an abundance fold change of greater than 2 (i.e., $\log_2$ difference < −1 or > 1) was required. Further assessment of potentially enriched protein categories was performed via 1D annotation enrichment (Benjamini-Hochberg FDR < 0.1) for the SN samples. The mass spectrometry proteomics data have been deposited to the ProteomeXchange Consortium (107) via the PRIDE partner repository with the data set identifier PXD049478.

Bioinformatics data analysis

For bioinformatics data analysis of protein aggregates, two different data sets were defined. All proteins, that were identified in at least two biological replicates of either wild-type or Δ*tisB* supernatant samples, were used as reference and referred to as combined supernatant. All proteins, that were exclusively present or enriched in wild-type pellet fractions in comparison to Δ*tisB* pellet fractions, were defined as TisB-dependent protein aggregates (TdPA). For the prediction of protein localization, LocTree3 was used (108). The file 83333_Escherichia_coli.bact.lc3 was retrieved from Bacteria.zip and used to assign the localization to each identified protein. For protein-protein association networks and functional enrichment analyses, a multi-protein search in the STRING database was performed (68).

ACKNOWLEDGMENTS

We are grateful to Niklas Philipp for his help with data analysis. We would like to thank Nasrine Bekhedda and Dana Sensen for their experimental support. Abram Aertsen is acknowledged for providing the *ibpA-msfGFP* reporter strain. We further thank Liliya Chernova for the discussion on protein aggregation and Kai Thormann for support with microscopy.

Work in the group of B.A.B. was supported by the German Research Council (DFG) in the framework of the SPP2002 (BE 5210/3-1 and BE 5210/3-2) and by Fonds der Chemischen Industrie (material cost allowance). A.T. and L.C. were supported by DFG in the framework of the SPP2002, project Z2 (TH872/10-2). H.-G.K. was supported by the DFG in the framework of the SPP2002 (KO2184/9.1 and KO2184/9.2) and by the SFB1381 (Project ID 403222702).

AUTHOR AFFILIATIONS

[1]Institute for Microbiology and Molecular Biology, Justus-Liebig-Universität, Giessen, Germany
[2]Systematic Proteome Research & Bioanalytics, Institute for Experimental Medicine, Christian-Albrechts-Universität, Kiel, Germany
[3]Branch for Bioresources of the Fraunhofer IME, Fraunhofer Institute for Molecular Biology and Applied Ecology IME, Giessen, Germany
[4]Department of Insect Biotechnology, Justus-Liebig-Universität, Giessen, Germany
[5]Bioinformatics and Systems Biology, Justus-Liebig-Universität, Giessen, Germany
[6]Institute of Biochemistry and Molecular Biology, ZBMZ, Faculty of Medicine, Albert-Ludwigs-Universität, Freiburg, Germany
[7]Faculty of Biology, Albert-Ludwigs-Universität, Freiburg, Germany
[8]Internal Medicine IV, Department of Medicine, University Medical Center, and Faculty of Medicine, Albert-Ludwigs-Universität, Freiburg, Germany
[9]BIOSS Centre for Biological Signalling Studies, Albert-Ludwigs-Universität, Freiburg, Germany

PRESENT ADDRESS

Bork A. Berghoff, Institute of Molecular Biology and Biotechnology of Prokaryotes, University of Ulm, Ulm, Germany

AUTHOR ORCIDs

Andreas Tholey http://orcid.org/0000-0002-8687-6817
Hans-Georg Koch http://orcid.org/0000-0001-5913-0334
Bork A. Berghoff http://orcid.org/0000-0002-6299-419X

FUNDING

Funder	Grant(s)	Author(s)
Deutsche Forschungsgemeinschaft (DFG)	BE 5210/3-1,BE 5210/3-2	Bork A. Berghoff
Fonds der Chemischen Industrie (FCI)	material cost allowance	Bork A. Berghoff
Deutsche Forschungsgemeinschaft (DFG)	TH872/10-2	Liam Cassidy Andreas Tholey
Deutsche Forschungsgemeinschaft (DFG)	KO2184/9.1, KO2184/9.2, SFB1381 (Project ID 403222702)	Hans-Georg Koch

AUTHOR CONTRIBUTIONS

Florian H. Leinberger, Conceptualization, Data curation, Formal analysis, Investigation, Validation, Visualization, Writing – original draft | Liam Cassidy, Data curation, Formal analysis, Investigation, Methodology, Validation, Visualization, Writing – original draft | Daniel Edelmann, Conceptualization, Formal analysis, Investigation | Nicole E. Schmid, Formal analysis, Investigation | Markus Oberpaul, Formal analysis, Investigation, Methodology | Patrick Blumenkamp, Data curation, Formal analysis | Sebastian Schmidt, Investigation | Ana Natriashvili, Formal analysis, Investigation | Maximilian H. Ulbrich, Data curation, Formal analysis, Methodology, Visualization | Andreas Tholey, Formal analysis, Funding acquisition, Project administration, Supervision | Hans-Georg Koch, Conceptualization, Funding acquisition, Project administration, Supervision | Bork A. Berghoff, Conceptualization, Formal analysis, Funding acquisition, Project administration, Supervision, Visualization, Writing – original draft

DATA AVAILABILITY

Processed RNA-seq data are available as Data Set S1 and have been deposited together with raw data files on the NCBI Gene Expression Omnibus (GEO) under the accession number GSE255764. The mass spectrometry proteomics data have been deposited to the ProteomeXchange Consortium (107) via the PRIDE partner repository with the data set identifier PXD049478.

ADDITIONAL FILES

The following material is available online.

Supplemental Material

Data Set S1 (mSystems01060-24-s0001.xlsx). RNA-seq results.
Data Set S2 (mSystems01060-24-s0002.xlsx). Proteomics data.
Supplemental Figures (mSystems01060-24-s0003.pdf). Figures S1 to S9.
Supplemental Tables (mSystems01060-24-s0004.xlsx). Tables S1 to S3.

REFERENCES

1. Ayrapetyan M, Williams T, Oliver JD. 2018. Relationship between the viable but nonculturable state and antibiotic persister cells. J Bacteriol 200:e00249-18. https://doi.org/10.1128/JB.00249-18
2. Lewis K. 2007. Persister cells, dormancy and infectious disease. Nat Rev Microbiol 5:48–56. https://doi.org/10.1038/nrmicro1557
3. Veening J-W, Smits WK, Kuipers OP. 2008. Bistability, epigenetics, and bet-hedging in bacteria. Annu Rev Microbiol 62:193–210. https://doi.org/10.1146/annurev.micro.62.081307.163002
4. McDonald MD, Owusu-Ansah C, Ellenbogen JB, Malone ZD, Ricketts MP, Frolking SE, Ernakovich JG, Ibba M, Bagby SC, Weissman JL. 2024. What is microbial dormancy? Trends Microbiol 32:142–150. https://doi.org/10.1016/j.tim.2023.08.006
5. Lennon JT, Jones SE. 2011. Microbial seed banks: the ecological and evolutionary implications of dormancy. Nat Rev Microbiol 9:119–130. https://doi.org/10.1038/nrmicro2504
6. Checinska A, Paszczynski A, Burbank M. 2015. *Bacillus* and other spore-forming genera: variations in responses and mechanisms for survival. Annu Rev Food Sci Technol 6:351–369. https://doi.org/10.1146/annurev-food-030713-092332
7. Muñoz-Dorado J, Marcos-Torres FJ, García-Bravo E, Moraleda-Muñoz A, Pérez J. 2016. Myxobacteria: moving, killing, feeding, and surviving together. Front Microbiol 7:781. https://doi.org/10.3389/fmicb.2016.00781
8. Lewis K. 2010. Persister cells. Annu Rev Microbiol 64:357–372. https://doi.org/10.1146/annurev.micro.112408.134306
9. Lewis K. 2008. Multidrug tolerance of biofilms and persister cells, p 107–131. In Current topics in microbiology and immunology
10. Balaban NQ, Helaine S, Lewis K, Ackermann M, Aldridge B, Andersson DI, Brynildsen MP, Bumann D, Camilli A, Collins JJ, Dehio C, Fortune S, Ghigo J-M, Hardt W-D, Harms A, Heinemann M, Hung DT, Jenal U, Levin BR, Michiels J, Storz G, Tan M-W, Tenson T, Van Melderen L, Zinkernagel A. 2019. Definitions and guidelines for research on antibiotic persistence. Nat Rev Microbiol 17:441–448. https://doi.org/10.1038/s41579-019-0196-3
11. Liu J, Gefen O, Ronin I, Bar-Meir M, Balaban NQ. 2020. Effect of tolerance on the evolution of antibiotic resistance under drug combinations. Science 367:200–204. https://doi.org/10.1126/science.aay3041
12. Levin-Reisman I, Ronin I, Gefen O, Braniss I, Shoresh N, Balaban NQ. 2017. Antibiotic tolerance facilitates the evolution of resistance. Science 355:826–830. https://doi.org/10.1126/science.aaj2191
13. Windels EM, Michiels JE, Fauvart M, Wenseleers T, Van den Bergh B, Michiels J. 2019. Bacterial persistence promotes the evolution of antibiotic resistance by increasing survival and mutation rates. ISME J 13:1239–1251. https://doi.org/10.1038/s41396-019-0344-9
14. Balaban NQ, Merrin J, Chait R, Kowalik L, Leibler S. 2004. Bacterial persistence as a phenotypic switch. Science 305:1622–1625. https://doi.org/10.1126/science.1099390
15. Johnson PJT, Levin BR. 2013. Pharmacodynamics, population dynamics, and the evolution of persistence in *Staphylococcus aureus*. PLoS Genet 9:e1003123. https://doi.org/10.1371/journal.pgen.1003123
16. Pontes MH, Groisman EA. 2019. Slow growth determines nonheritable antibiotic resistance in *Salmonella enterica*. Sci Signal 12:eaax3938. https://doi.org/10.1126/scisignal.aax3938
17. Korch SB, Henderson TA, Hill TM. 2003. Characterization of the *hipA7* allele of *Escherichia coli* and evidence that high persistence is governed

by (p)ppGpp synthesis. Mol Microbiol 50:1199–1213. https://doi.org/10.1046/j.1365-2958.2003.03779.x
18. Radzikowski JL, Vedelaar S, Siegel D, Ortega ÁD, Schmidt A, Heinemann M. 2016. Bacterial persistence is an active σ^S stress response to metabolic flux limitation. Mol Syst Biol 12:882. https://doi.org/10.15252/msb.20166998
19. Wu Y, Vulić M, Keren I, Lewis K. 2012. Role of oxidative stress in persister tolerance. Antimicrob Agents Chemother 56:4922–4926. https://doi.org/10.1128/AAC.00921-12
20. Hernandez-Morfa M, Reinoso-Vizcaíno NM, Olivero NB, Zappia VE, Cortes PR, Jaime A, Echenique J. 2022. Host cell oxidative stress promotes intracellular fluoroquinolone persisters of *Streptococcus pneumoniae*. Microbiol Spectr 10:e0436422. https://doi.org/10.1128/spectrum.04364-22
21. Shan Y, Brown Gandt A, Rowe SE, Deisinger JP, Conlon BP, Lewis K. 2017. ATP-dependent persister formation in *Escherichia coli*. mBio 8:e02267-16. https://doi.org/10.1128/mBio.02267-16
22. Conlon BP, Rowe SE, Gandt AB, Nuxoll AS, Donegan NP, Zalis EA, Clair G, Adkins JN, Cheung AL, Lewis K. 2016. Persister formation in *Staphylococcus aureus* is associated with ATP depletion. Nat Microbiol 1:16051. https://doi.org/10.1038/nmicrobiol.2016.51
23. Orman MA, Brynildsen MP. 2013. Dormancy is not necessary or sufficient for bacterial persistence. Antimicrob Agents Chemother 57:3230–3239. https://doi.org/10.1128/AAC.00243-13
24. Harms A, Brodersen DE, Mitarai N, Gerdes K. 2018. Toxins, targets, and triggers: an overview of toxin-antitoxin biology. Mol Cell 70:768–784. https://doi.org/10.1016/j.molcel.2018.01.003
25. Jurėnas D, Fraikin N, Goormaghtigh F, Van Melderen L. 2022. Biology and evolution of bacterial toxin-antitoxin systems. Nat Rev Microbiol 20:335–350. https://doi.org/10.1038/s41579-021-00661-1
26. Ronneau S, Helaine S. 2019. Clarifying the link between toxin–antitoxin modules and bacterial persistence. J Mol Biol 431:3462–3471. https://doi.org/10.1016/j.jmb.2019.03.019
27. Shore SFH, Leinberger FH, Fozo EM, Berghoff BA. 2024. Type I toxin-antitoxin systems in bacteria: from regulation to biological functions. EcoSal Plus:eesp00252022. https://doi.org/10.1128/ecosalplus.esp-0025-2022
28. Page R, Peti W. 2016. Toxin-antitoxin systems in bacterial growth arrest and persistence. Nat Chem Biol 12:208–214. https://doi.org/10.1038/nchembio.2044
29. Van Melderen L, Wood TK. 2017. Commentary: what is the link between stringent response, endoribonuclease encoding type II toxin-antitoxin systems and persistence? Front Microbiol 8:191. https://doi.org/10.3389/fmicb.2017.00191
30. Goormaghtigh F, Fraikin N, Putrinš M, Hallaert T, Hauryliuk V, Garcia-Pino A, Sjödin A, Kasvandik S, Udekwu K, Tenson T, Kaldalu N, Van Melderen L. 2018. Reassessing the role of type II toxin-antitoxin systems in formation of *Escherichia coli* type II persister cells. mBio 9:e00640-18. https://doi.org/10.1128/mBio.00640-18
31. Edelmann D, Berghoff BA. 2022. A shift in perspective: a role for the type I toxin TisB as persistence-stabilizing factor. Front Microbiol 13:871699. https://doi.org/10.3389/fmicb.2022.871699
32. Helaine S, Cheverton AM, Watson KG, Faure LM, Matthews SA, Holden DW. 2014. Internalization of *Salmonella* by macrophages induces formation of nonreplicating persisters. Science 343:204–208. https://doi.org/10.1126/science.1244705
33. Dörr T, Vulić M, Lewis K. 2010. Ciprofloxacin causes persister formation by inducing the TisB toxin in *Escherichia coli*. PLoS Biol 8:e1000317. https://doi.org/10.1371/journal.pbio.1000317
34. Wagner EGH, Unoson C. 2012. The toxin-antitoxin system *tisB-istR1*: expression, regulation, and biological role in persister phenotypes. RNA Biol 9:1513–1519. https://doi.org/10.4161/rna.22578
35. Berghoff BA, Wagner EGH. 2019. Persister formation driven by TisB-dependent membrane depolarization, p 77–97. In Lewis K (ed), Persister cells and infectious disease. Springer International Publishing, Cham.
36. Berghoff BA, Wagner EGH. 2017. RNA-based regulation in type I toxin-antitoxin systems and its implication for bacterial persistence. Curr Genet 63:1011–1016. https://doi.org/10.1007/s00294-017-0710-y
37. Unoson C, Wagner EGH. 2008. A small SOS-induced toxin is targeted against the inner membrane in *Escherichia coli*. Mol Microbiol 70:258–270. https://doi.org/10.1111/j.1365-2958.2008.06416.x
38. Gurnev PA, Ortenberg R, Dörr T, Lewis K, Bezrukov SM. 2012. Persister-promoting bacterial toxin TisB produces anion-selective pores in planar lipid bilayers. FEBS Lett 586:2529–2534. https://doi.org/10.1016/j.febslet.2012.06.021
39. Berghoff BA, Hoekzema M, Aulbach L, Wagner EGH. 2017. Two regulatory RNA elements affect TisB-dependent depolarization and persister formation. Mol Microbiol 103:1020–1033. https://doi.org/10.1111/mmi.13607
40. Edelmann D, Berghoff BA. 2019. Type I toxin-dependent generation of superoxide affects the persister life cycle of *Escherichia coli*. Sci Rep 9:14256. https://doi.org/10.1038/s41598-019-50668-1
41. Berghoff BA, Karlsson T, Källman T, Wagner EGH, Grabherr MG. 2017. RNA-sequence data normalization through *in silico* prediction of reference genes: the bacterial response to DNA damage as case study. BioData Min 10:30. https://doi.org/10.1186/s13040-017-0150-8
42. Vogel J, Argaman L, Wagner EGH, Altuvia S. 2004. The small RNA IstR inhibits synthesis of an SOS-induced toxic peptide. Curr Biol 14:2271–2276. https://doi.org/10.1016/j.cub.2004.12.003
43. Darfeuille F, Unoson C, Vogel J, Wagner EGH. 2007. An antisense RNA inhibits translation by competing with standby ribosomes. Mol Cell 26:381–392. https://doi.org/10.1016/j.molcel.2007.04.003
44. Romilly C, Lippegaus A, Wagner EGH. 2020. An RNA pseudoknot is essential for standby-mediated translation of the *tisB* toxin mRNA in *Escherichia coli*. Nucleic Acids Res 48:12336–12347. https://doi.org/10.1093/nar/gkaa1139
45. Romilly C, Deindl S, Wagner EGH. 2019. The ribosomal protein S1-dependent standby site in *tisB* mRNA consists of a single-stranded region and a 5′ structure element. Proc Natl Acad Sci U S A 116:15901–15906. https://doi.org/10.1073/pnas.1904309116
46. Edelmann D, Oberpaul M, Schäberle TF, Berghoff BA. 2021. Post-transcriptional deregulation of the *tisB/istR-1* toxin–antitoxin system promotes SOS-independent persister formation in *Escherichia coli*. Environ Microbiol Rep 13:159–168. https://doi.org/10.1111/1758-2229.12919
47. Fozo EM, Kawano M, Fontaine F, Kaya Y, Mendieta KS, Jones KL, Ocampo A, Rudd KE, Storz G. 2008. Repression of small toxic protein synthesis by the Sib and OhsC small RNAs. Mol Microbiol 70:1076–1093. https://doi.org/10.1111/j.1365-2958.2008.06394.x
48. Brielle R, Pinel-Marie M-L, Felden B. 2016. Linking bacterial type I toxins with their actions. Curr Opin Microbiol 30:114–121. https://doi.org/10.1016/j.mib.2016.01.009
49. Spanka D-T, Konzer A, Edelmann D, Berghoff BA. 2019. High-throughput proteomics identifies proteins with importance to postantibiotic recovery in depolarized persister cells. Front Microbiol 10:378. https://doi.org/10.3389/fmicb.2019.00378
50. Edelmann D, Leinberger FH, Schmid NE, Oberpaul M, Schäberle TF, Berghoff BA. 2021. Elevated expression of toxin TisB protects persister cells against ciprofloxacin but enhances susceptibility to mitomycin C. Microorganisms 9:943. https://doi.org/10.3390/microorganisms9050943
51. Lutz R, Bujard H. 1997. Independent and tight regulation of transcriptional units in *Escherichia coli* via the LacR/O, the TetR/O and AraC/I1-I2 regulatory elements. Nucleic Acids Res 25:1203–1210. https://doi.org/10.1093/nar/25.6.1203
52. Osterman IA, Evfratov SA, Sergiev PV, Dontsova OA. 2013. Comparison of mRNA features affecting translation initiation and reinitiation. Nucleic Acids Res 41:474–486. https://doi.org/10.1093/nar/gks989
53. Rotem E, Loinger A, Ronin I, Levin-Reisman I, Gabay C, Shoresh N, Biham O, Balaban NQ. 2010. Regulation of phenotypic variability by a threshold-based mechanism underlies bacterial persistence. Proc Natl Acad Sci U S A 107:12541–12546. https://doi.org/10.1073/pnas.1004333107
54. Levin-Reisman I, Fridman O, Balaban NQ. 2014. ScanLag: high-throughput quantification of colony growth and lag time. J Vis Exp e51456:51456. https://doi.org/10.3791/51456
55. Levin-Reisman I, Gefen O, Fridman O, Ronin I, Shwa D, Sheftel H, Balaban NQ. 2010. Automated imaging with ScanLag reveals previously

undetectable bacterial growth phenotypes. Nat Methods 7:737–739. https://doi.org/10.1038/nmeth.1485
56. Santos-Zavaleta A, Salgado H, Gama-Castro S, Sánchez-Pérez M, Gómez-Romero L, Ledezma-Tejeida D, García-Sotelo JS, Alquicira-Hernández K, Muñiz-Rascado LJ, Peña-Loredo P, Ishida-Gutiérrez C, Velázquez-Ramírez DA, Del Moral-Chávez V, Bonavides-Martínez C, Méndez-Cruz CF, Galagan J, Collado-Vides J. 2019. RegulonDB v 10.5: tackling challenges to unify classic and high throughput knowledge of gene regulation in *E. coli* K-12. Nucleic Acids Res 47:D212–D220. https://doi.org/10.1093/nar/gky1077
57. Grabowicz M, Silhavy TJ. 2017. Envelope stress responses: an interconnected safety net. Trends Biochem Sci 42:232–242. https://doi.org/10.1016/j.tibs.2016.10.002
58. Lee J, Hiibel SR, Reardon KF, Wood TK. 2010. Identification of stress - related proteins in *Escherichia coli* using the pollutant *cis* - dichloroethylene. J Appl Microbiol 108:2088–2102. https://doi.org/10.1111/j.1365-2672.2009.04611.x
59. Zhang X-S, García-Contreras R, Wood TK. 2007. YcfR (BhsA) influences *Escherichia coli* biofilm formation through stress response and surface hydrophobicity. J Bacteriol 189:3051–3062. https://doi.org/10.1128/JB.01832-06
60. Mermod M, Magnani D, Solioz M, Stoyanov JV. 2012. The copper-inducible ComR (YcfQ) repressor regulates expression of ComC (YcfR), which affects copper permeability of the outer membrane of *Escherichia coli*. Biometals 25:33–43. https://doi.org/10.1007/s10534-011-9510-x
61. Zhao Z, Xu Y, Jiang B, Qi Q, Tang Y-J, Xian M, Wang J, Zhao G. 2022. Systematic identification of CpxRA-regulated genes and their roles in *Escherichia coli* stress response. mSystems 7:e0041922. https://doi.org/10.1128/msystems.00419-22
62. Pu Y, Li Y, Jin X, Tian T, Ma Q, Zhao Z, Lin S-Y, Chen Z, Li B, Yao G, Leake MC, Lo C-J, Bai F. 2019. ATP-dependent dynamic protein aggregation regulates bacterial dormancy depth critical for antibiotic tolerance. Mol Cell 73:143–156. https://doi.org/10.1016/j.molcel.2018.10.022
63. Dewachter L, Bollen C, Wilmaerts D, Louwagie E, Herpels P, Matthay P, Khodaparast L, Khodaparast L, Rousseau F, Schymkowitz J, Michiels J. 2021. The dynamic transition of persistence toward the viable but nonculturable state during stationary phase is driven by protein aggregation. mBio 12:e0070321. https://doi.org/10.1128/mBio.00703-21
64. Govers SK, Mortier J, Adam A, Aertsen A. 2018. Protein aggregates encode epigenetic memory of stressful encounters in individual *Escherichia coli* cells. PLoS Biol 16:e2003853. https://doi.org/10.1371/journal.pbio.2003853
65. Falk T, Mai D, Bensch R, Çiçek Ö, Abdulkadir A, Marrakchi Y, Böhm A, Deubner J, Jäckel Z, Seiwald K, Dovzhenko A, Tietz O, Dal Bosco C, Walsh S, Saltukoglu D, Tay TL, Prinz M, Palme K, Simons M, Diester I, Brox T, Ronneberger O. 2019. U-Net: deep learning for cell counting, detection, and morphometry. Nat Methods 16:67–70. https://doi.org/10.1038/s41592-018-0261-2
66. Courcelle J, Khodursky A, Peter B, Brown PO, Hanawalt PC. 2001. Comparative gene expression profiles following UV exposure in wild-type and SOS-deficient *Escherichia coli*. Genetics 158:41–64. https://doi.org/10.1093/genetics/158.1.41
67. Wagner S, Baars L, Ytterberg AJ, Klussmeier A, Wagner CS, Nord O, Nygren P-A, van Wijk KJ, de Gier J-W. 2007. Consequences of membrane protein overexpression in *Escherichia coli*. Mol Cell Proteomics 6:1527–1550. https://doi.org/10.1074/mcp.M600431-MCP200
68. Szklarczyk D, Kirsch R, Koutrouli M, Nastou K, Mehryary F, Hachilif R, Gable AL, Fang T, Doncheva NT, Pyysalo S, Bork P, Jensen LJ, von Mering C. 2023. The STRING database in 2023: protein-protein association networks and functional enrichment analyses for any sequenced genome of interest. Nucleic Acids Res 51:D638–D646. https://doi.org/10.1093/nar/gkac1000
69. Harrison JJ, Wade WD, Akierman S, Vacchi-Suzzi C, Stremick CA, Turner RJ, Ceri H. 2009. The chromosomal toxin gene *yafQ* is a determinant of multidrug tolerance for *Escherichia coli* growing in a biofilm. Antimicrob Agents Chemother 53:2253–2258. https://doi.org/10.1128/AAC.00043-09
70. Singh R, Barry CE, Boshoff HIM. 2010. The three RelE homologs of *Mycobacterium tuberculosis* have individual, drug-specific effects on bacterial antibiotic tolerance. J Bacteriol 192:1279–1291. https://doi.org/10.1128/JB.01285-09
71. Korch SB, Hill TM. 2006. Ectopic overexpression of wild-type and mutant *hipA* genes in *Escherichia coli*: effects on macromolecular synthesis and persister formation. J Bacteriol 188:3826–3836. https://doi.org/10.1128/JB.01740-05
72. Chowdhury N, Kwan BW, Wood TK. 2016. Persistence increases in the absence of the alarmone guanosine tetraphosphate by reducing cell growth. Sci Rep 6:20519. https://doi.org/10.1038/srep20519
73. Ludwig P, Huber M, Lehr M, Wegener M, Zerulla K, Lange C, Soppa J. 2018. Non-canonical *Escherichia coli* transcripts lacking a Shine–Dalgarno motif have very different translational efficiencies and do not form a coherent group. Microbiol (Reading) 164:646–658. https://doi.org/10.1099/mic.0.000619
74. Mutschler H, Gebhardt M, Shoeman RL, Meinhart A. 2011. A novel mechanism of programmed cell death in bacteria by toxin-antitoxin systems corrupts peptidoglycan synthesis. PLoS Biol 9:e1001033. https://doi.org/10.1371/journal.pbio.1001033
75. Bahassi EM, O'Dea MH, Allali N, Messens J, Gellert M, Couturier M. 1999. Interactions of CcdB with DNA gyrase. Inactivation of GyrA, poisoning of the gyrase-DNA complex, and the antidote action of CcdA. J Biol Chem 274:10936–10944. https://doi.org/10.1074/jbc.274.16.10936
76. Critchlow SE, O'Dea MH, Howells AJ, Couturier M, Gellert M, Maxwell A. 1997. The interaction of the F plasmid killer protein, CcdB, with DNA gyrase: induction of DNA cleavage and blocking of transcription. J Mol Biol 273:826–839. https://doi.org/10.1006/jmbi.1997.1357
77. Wilmaerts D, Dewachter L, De Loose P-J, Bollen C, Verstraeten N, Michiels J. 2019. HokB monomerization and membrane repolarization control persister awakening. Mol Cell 75:1031–1042. https://doi.org/10.1016/j.molcel.2019.06.015
78. Schramm FD, Schroeder K, Jonas K. 2020. Protein aggregation in bacteria. FEMS Microbiol Rev 44:54–72. https://doi.org/10.1093/femsre/fuz026
79. Mogk A, Bukau B, Kampinga HH. 2018. Cellular handling of protein aggregates by disaggregation machines. Mol Cell 69:214–226. https://doi.org/10.1016/j.molcel.2018.01.004
80. He W, Yu G, Li T, Bai L, Yang Y, Xue Z, Pang Y, Reichmann D, Hiller S, He L, Liu M, Quan S. 2021. Chaperone spy protects outer membrane proteins from folding stress via dynamic complex formation. mBio 12:e0213021. https://doi.org/10.1128/mBio.02130-21
81. Mitra R, Wu K, Lee C, Bardwell JCA. 2022. ATP-independent chaperones. Annu Rev Biophys 51:409–429. https://doi.org/10.1146/annurev-biophys-090121-082906
82. DiGiuseppe PA, Silhavy TJ. 2003. Signal detection and target gene induction by the CpxRA two-component system. J Bacteriol 185:2432–2440. https://doi.org/10.1128/JB.185.8.2432-2440.2003
83. Wu X, Held K, Zheng C, Staudinger BJ, Chavez JD, Weisbrod CR, Eng JK, Singh PK, Manoil C, Bruce JE. 2015. Dynamic proteome response of *Pseudomonas aeruginosa* to tobramycin antibiotic treatment. Mol Cell Proteomics 14:2126–2137. https://doi.org/10.1074/mcp.M115.050161
84. Tran TDH, Kwon HY, Kim EH, Kim KW, Briles DE, Pyo S, Rhee DK. 2011. Decrease in penicillin susceptibility due to heat shock protein ClpL in *Streptococcus pneumoniae*. Antimicrob Agents Chemother 55:2714–2728. https://doi.org/10.1128/AAC.01383-10
85. Cardoso K, Gandra RF, Wisniewski ES, Osaku CA, Kadowaki MK, Felipach-Neto V, Haus L-Á, Simão R de C. 2010. DnaK and GroEL are induced in response to antibiotic and heat shock in *Acinetobacter baumannii*. J Med Microbiol 59:1061–1068. https://doi.org/10.1099/jmm.0.020339-0
86. Yamaguchi Y, Tomoyasu T, Takaya A, Morioka M, Yamamoto T. 2003. Effects of disruption of heat shock genes on susceptibility of *Escherichia coli* to fluoroquinolones. BMC Microbiol 3:1–8. https://doi.org/10.1186/1471-2180-3-16
87. Khodaparast L, Khodaparast L, Gallardo R, Louros NN, Michiels E, Ramakrishnan R, Ramakers M, Claes F, Young L, Shahrooei M, Wilkinson H, Desager M, Mengistu Tadesse W, Nilsson KPR, Hammarström P, Aertsen A, Carpentier S, Van Eldere J, Rousseau F, Schymkowitz J. 2018. Aggregating sequences that occur in many proteins constitute weak

spots of bacterial proteostasis. Nat Commun 9:866. https://doi.org/10.1038/s41467-018-03131-0
88. Michels M, Bakker EP. 1985. Generation of a large, protonophore-sensitive proton motive force and pH difference in the acidophilic bacteria *Thermoplasma acidophilum* and *Bacillus acidocaldarius*. J Bacteriol 161:231–237. https://doi.org/10.1128/jb.161.1.231-237.1985
89. Krulwich TA, Sachs G, Padan E. 2011. Molecular aspects of bacterial pH sensing and homeostasis. Nat Rev Microbiol 9:330–343. https://doi.org/10.1038/nrmicro2549
90. Cayron J, Oms T, Schlechtweg T, Zedek S, Van Melderen L. 2024. TisB protein is the single molecular determinant underlying multiple downstream effects of ofloxacin in *Escherichia coli*. Sci Adv 10:eadk1577. https://doi.org/10.1126/sciadv.adk1577
91. Van Tartwijk FW, Kaminski CF. 2022. Protein condensation, cellular organization, and spatiotemporal regulation of cytoplasmic properties. Adv Biol 6:e2101328. https://doi.org/10.1002/adbi.202101328
92. Wang X, Kim Y, Ma Q, Hong SH, Pokusaeva K, Sturino JM, Wood TK. 2010. Cryptic prophages help bacteria cope with adverse environments. Nat Commun 1:147. https://doi.org/10.1038/ncomms1146
93. Jõers A, Kaldalu N, Tenson T. 2010. The frequency of persisters in *Escherichia coli* reflects the kinetics of awakening from dormancy. J Bacteriol 192:3379–3384. https://doi.org/10.1128/JB.00056-10
94. Goormaghtigh F, Van Melderen L. 2019. Single-cell imaging and characterization of *Escherichia coli* persister cells to ofloxacin in exponential cultures. Sci Adv 5:eaav9462. https://doi.org/10.1126/sciadv.aav9462
95. Datsenko KA, Wanner BL. 2000. One-step inactivation of chromosomal genes in *Escherichia coli* K-12 using PCR products. Proc Natl Acad Sci U S A 97:6640–6645. https://doi.org/10.1073/pnas.120163297
96. Datta S, Costantino N, Court DL. 2006. A set of recombineering plasmids for Gram-negative bacteria. Gene 379:109–115. https://doi.org/10.1016/j.gene.2006.04.018
97. Beyer HM, Gonschorek P, Samodelov SL, Meier M, Weber W, Zurbriggen MD. 2015. AQUA cloning: a versatile and simple enzyme-free cloning approach. PLoS One 10:e0137652. https://doi.org/10.1371/journal.pone.0137652
98. Köbel TS, Melo Palhares R, Fromm C, Szymanski W, Angelidou G, Glatter T, Georg J, Berghoff BA, Schindler D. 2022. An easy-to-use plasmid toolset for efficient generation and benchmarking of synthetic small RNAs in bacteria. ACS Synth Biol 11:2989–3003. https://doi.org/10.1021/acssynbio.2c00164
99. Ewels P, Magnusson M, Lundin S, Käller M. 2016. MultiQC: summarize analysis results for multiple tools and samples in a single report. Bioinformatics 32:3047–3048. https://doi.org/10.1093/bioinformatics/btw354
100. Langmead B, Salzberg SL. 2012. Fast gapped-read alignment with Bowtie 2. Nat Methods 9:357–359. https://doi.org/10.1038/nmeth.1923
101. Danecek P, Bonfield JK, Liddle J, Marshall J, Ohan V, Pollard MO, Whitwham A, Keane T, McCarthy SA, Davies RM, Li H. 2021. Twelve years of SAMtools and BCFtools. Gigascience 10:1–4. https://doi.org/10.1093/gigascience/giab008
102. Liao Y, Smyth GK, Shi W. 2014. featureCounts: an efficient general purpose program for assigning sequence reads to genomic features. Bioinformatics 30:923–930. https://doi.org/10.1093/bioinformatics/btt656
103. Love MI, Huber W, Anders S. 2014. Moderated estimation of fold change and dispersion for RNA-seq data with DESeq2. Genome Biol 15:550. https://doi.org/10.1186/s13059-014-0550-8
104. Pfaffl MW. 2001. A new mathematical model for relative quantification in real-time RT-PCR. Nucleic Acids Res 29:e45. https://doi.org/10.1093/nar/29.9.e45
105. Schägger H. 2006. Tricine–SDS-PAGE. Nat Protoc 1:16–22. https://doi.org/10.1038/nprot.2006.4
106. Hughes CS, Moggridge S, Müller T, Sorensen PH, Morin GB, Krijgsveld J. 2019. Single-pot, solid-phase-enhanced sample preparation for proteomics experiments. Nat Protoc 14:68–85. https://doi.org/10.1038/s41596-018-0082-x
107. Vizcaíno JA, Deutsch EW, Wang R, Csordas A, Reisinger F, Ríos D, Dianes JA, Sun Z, Farrah T, Bandeira N, Binz PA, Xenarios I, Eisenacher M, Mayer G, Gatto L, Campos A, Chalkley RJ, Kraus HJ, Albar JP, Martinez-Bartolomé S, Apweiler R, Omenn GS, Martens L, Jones AR, Hermjakob H. 2014. ProteomeXchange provides globally coordinated proteomics data submission and dissemination. Nat Biotechnol 32:223–226. https://doi.org/10.1038/nbt.2839
108. Goldberg T, Hecht M, Hamp T, Karl T, Yachdav G, Ahmed N, Altermann U, Angerer P, Ansorge S, Balasz K, et al. 2014. LocTree3 prediction of localization. Nucleic Acids Res 42:W350–W355. https://doi.org/10.1093/nar/gku396